C3N Monolayer: Exploring the Emerging of Novel Electronic and Magnetic Properties with Adatom Adsorption, Functionalizations, Electric Field, Charging, and Strain
— **Source link** ↗

Asadollah Bafekry, Asadollah Bafekry, Saber Farjami Shayesteh, François M. Peeters

Institutions: University of Antwerp, University of Gilan

Topics: Band gap, Monolayer and Polyaniline

Related papers:

- Generalized Gradient Approximation Made Simple

- Special points for brillouin-zone integrations

- Introducing novel electronic and magnetic properties in C3N nanosheets by defect engineering and atom substitution.

- Ultra high stiffness and thermal conductivity of graphene like C3N

- Two-dimensional polyaniline (C3N) from carbonized organic single crystals in solid state

Universiteit Antwerpen

This item is the archived peer-reviewed author-version of:

C3N monolayer : exploring the emerging of novel electronic and magnetic properties with adatom adsorption, functionalizations, electric field, charging, and strain

uantwerpen.be

CN Monolayer: Exploring the Emerging of Novel Electronic and Magnetic Properties with Adatom Adsorption, Functionalizations, Electric Field, Charging and Strain

Asadollah Bafekry, Saber Farjami Shayesteh, and Francois M. Peeters

Just Accepted

C_3N Monolayer: Exploring the Emerging of Novel Electronic and Magnetic Properties with Adatom Adsorption, Functionalizations, Electric Field, Charging and Strain

Asadollah Bafekry,[*,†,‡] Saber Farjami Shayesteh,[†] and Francois M. Peeters[‡]

†*Department of Physics, University of Guilan, 41335-1914 Rasht, Iran*

‡*Department of Physics, University of Antwerp, Groenenborgerlaan 171, B-2020 Antwerp,*

Belgium

E-mail: Bafekry.asad@gmail.com

Abstract

Two-dimensional polyaniline (2D PANI) with structural unit C_3N is an indirect semiconductor with 0.4 eV band gap, which has attracted a lot of interest because of its unusual electronic, optoelectronic, thermal and mechanical properties useful for various applications. Adsorption of adatoms is an effective method to improve and tune the properties of C_3N. Using first-principles calculations we investigated the adsorption of adatoms including H, O, S, ,F , Cl, B, C, Si, N, P, Al, Li, Na, K, Be, Mg, Ca, Sc, Ti, V, Cr, Mn, Fe, Co, Ni, Cu and Zn on C_3N. Depending on the adatom size and the number of valence electrons they may induce metallic, half-metallic, semiconducting and ferromagnetic-metallic behavior. In addition, we investigate the effects of an electrical field, charging and strain on C_3N and found how the electronic and magnetic properties are modified. Semi and fully hydrogenation, are studied. From the mechanical and

thermal stability of C_3N monolayer, we found it to be a hard material which can withstand large strain. From our calculations we gained novel insights into the properties of C_3N demonstrating its unique electronic and magnetic properties that can be useful for semiconducting, nanosensor and catalytic applications.

Introduction

Progress in synthesis and characterization of nanostructural of materials, have opened up important possibilities for the research of two-dimensional materials (2DM). Graphene[1] as a single layer honeycomb lattice of carbon atoms, has attracted a surge of interest due to their unusual properties[2–6] and numerous potential applications in various fields such as catalysis, energy storage, optoelectronic devices, spintronics and sensors.[7–15] Due to the lack of a band gap in graphene, a lot of research efforts has gone towards the investigation of how a band gap can be artificially induced.[16–19] Recent studies have demonstrated, that adatom adsorption may open a bandgap in its electronic structure[20–22] and also may lead to the emergence of magnetism in graphene[23] with potential applications.[24,25] Several computational studies have been conducted to investigate adatom adsorption on 2D monolayers.[26–31]

2DM including hexagonal boron-nitride (h-BN), and transition metal dichalcogenides have been extracted from layered bulk materials. These monolayer atomic structures exhibit unique physical properties quite distinct from their original 3D bulk structures.[6,32–34] Several monolayers from group IV elements, such as silicene, germanene, and stanene, have been synthesized.[35–38] Transition metal dichalcogenides (TMDCs) with optical adsorption in the visible range are suitable as field effect transistors (FET), solar cells and photo-catalysis applications.[39,40] MXenes, a family of complex layered materials, are candidate for electrode material for various electrochemical energy storage devices including lithium-ion, sodium-ion batteries and supercapacitors.[41–43] In spite of the fact that 2DM hold great potential for a wide usage of applications, it will be necessary to modulate their intrinsic properties to transfer them into real applications. In recent years, several approaches have been developed

to modify the electronic and magnetic properties of 2DM. These methods involve substitutional doping, defect engineering, surface functionalization with adatoms, and application of an electric field.[44–49] From another perspective, the properties of 2DM can be modulated by strain engineering which does not involve any complicated chemical processing.[50,51]

Most recently, 2D polyaniline with stoichiometric formula C_3N and a graphene-like structure in which nitrogen is uniformly distributed has been successfully synthesized.[52] C_3N is predicted to offer a variety of applications such as solar cell devices, electrolyte gating and doping of transistors and anode material.[53–55] The single layer C_3N, was first reported to be an indirect band-gap semiconductor and three possible planar structures were suggested.[56,57] It exhibits ferromagnetic order at low temperatures when doped with hydrogen atoms.[58] The electronic structure of monolayer C_3N is give in Refs.[52,56,57,59]

Theoretical studies showed that C_3N exhibits ultrahigh stiffness and thermal conductivity.[60] Furthermore, DFT calculations showed that the electronic properties of C_3N can be tuned by adatom adsorption.[61–64] In this work we present an extensive analysis and consider adsorption of 27 adatoms such as, Al, alkali metal(AM) (Li, Na, K), alkaline earth metal (AEM) (Be, Mg and Ca) and 3d transition metal(TM) (Sc, Ti, V, Cr, Mn, Fe, Co, Ni, Cu and Zn) elements, and nonmetallic adatoms such as H, B, C, N, O, F, and P on the structural, electronic and magnetic properties of C_3N. Each adatom can be adsorbed at six stable adsorption sites within a 2×2 supercell of C_3N. We found that H, O, S, F and Cl adatoms are adsorbed at stable T_C-site and B, C, Si, N, P and Cu preferentially at B_{CC}-site, while other adatoms at H_{CC}-site. In conclusion, while C_3N is a nonmagnetic semiconductor, its band gap can be modulated through adatom adsorption. In specific cases C_3N attains its magnetic properties and becomes metallic and the adsorbed adatoms give rise to donor or acceptor states in the band gap. In addition we investigate the effects of charging, electrical field, strain and adatoms coverage on the properties of C_3N and Ad/C_3N. Some of these properties can be useful and very promising for future applications.

Method

We choose the OpenMX code[65,66] for our calculations which is one of the fastest DFT codes. It can quickly perform structural optimization of molecular structures using atomic orbital basis (PAO) sets and pseudopotential method, which can simulate a wide range of properties of crystals and surfaces of materials such as semiconductors, ceramics, metals and minerals. In this paper, we performed first-principles total energy and electronic structure calculations, within the Perdew-Burke-Ernzerhof variant of the generalized gradient approximation (PBE-GGA)[67] method, to deal with the exchange-correlation functionals. We used norm-conserving pseudopotentials,[68] for carbon, nitrogen and adatoms. The wave functions are expanded in a linear combination of multiple pseudoatomic orbitals (LCPAOs) generated by using a confinement scheme.[65,66] In the first step, the atomic structure positions in the C_3N and Ad/C_3N are optimized using OpenMX, which implements a quasi-Newton algorithm for atomic force relaxation. The geometries were fully relaxed with force acting on each atom less than 1 meV/Å. The K-points for sampling over the Brillouin zone (BZ) integration were generated using the Monkhorst-Pack scheme.[69] For a primitive cell of hexagonal C_3N, a K-mesh grid of $15 \times 15 \times 1$ was used. After the convergence tests in OpenMX, we chose cutoffs of 250 Ry for C_3N, so that the total-energies converge below 1.0 meV/atom. With these parameters the resulting structures are found to be sufficiently relaxed to obtain various properties in the next steps of the calculation. The charge transfer was calculated using the Mulliken charge analysis.[70]

Furthermore, we used the PW basis set with QUANTUM ESPRESSO[71] code, with kinetic energy cutoffs of 40 Ry and 320 Ry for the wave-functions and charge densities, with convergence in the total energy below 1.0 meV/atom. All atomic positions and lattice constants are optimized by using the conjugate gradient method, where the total energy and atomic forces are minimized. The convergence for total energy difference is less than 10^{-6} Ry between two steps, and the maximum force allowed on each atom is less than 10^{-3} a.u. between subsequent iterations. The Brillouin zone (BZ) is sampled by K-mesh grid of

4

$23 \times 23 \times 1$ for primitive unit cell and scaled according to the size of the supercells. The large difference in the numbers of k-points in the PW and PAO basis sets is due to the different symmetrization treatments in the programs.

In addition calculations within SIESTA code[72] are performed where the eigenstates of the Kohn-Sham Hamiltonian are expressed as linear combinations of numerical atomic orbitals. The exchange-correlation functional of the GGA-PBE was used. A 200 Ry mesh cut-off is chosen and the self-consistent calculations are performed with a mixing rate of 0.1. Core electrons are replaced by norm-conserving, nonlocal Troullier-Martins pseudopotential. The convergence criterion for the density matrix is taken as 10^{-4} Ry. The C_3N are modeled as a periodic slab with a sufficiently large vacuum layer (20 Å) in order to avoid interaction between adjacent layers. In order to accurately describe the vdW interaction in the C_3N, we adopted the empirical correction method presented by Grimme (DFT-D2), which had been proven reliable for describing the long-range vdW interactions.[73] In order to reveal whether the adsorbed adatoms can diffuse or migrate, we investigate the energy barriers for the displacement of the adatoms. The barrier is estimated through the Nudged Elastic Band (NEB) method.[74] In short, the NEB method allows for the determination of a minimum energy path (MEP) for the reaction pathway between two optimized structures by the use of images connected by fictitious springs. Simulated scanning tunneling microscopy (STM) images were obtained using the Tersoff-Hamann theory[75] for STM images, as supplied with OpenMX code. The STM simulated images are given for bias of $+2.0$ V (unoccupied states) and were graphed using WSxM software.[76] We performed molecular dynamics simulations at 500, 1000 and 1500 K temperatures for adatom prototypes with C_3N, to ensure that the adsorbed adatom on C_3N are thermodynamically stable.

Pristine C$_3$N

The honeycomb atomic structure of C$_3$N is a planar lattice which contains eight atoms (6 C and 2 N atoms) and can be regarded as a 2×2 supercell of graphene with two C substituted by two N atoms, as shown in Fig. 1(a). The optimized lattice constant of C$_3$N is 4.861 Å, which agrees well with the experimental value of 4.75 Å[52] and the C-C(d_{CC}) and C-N (d_{NC}) bond lengths are, 1.404 and 1.403 Å respectively, which agrees with previous theoretical calculations.[56,60–62] The total and difference charge densities are shown in Fig. 1(a). Notice that a high charge density is found around the N atoms. The difference charge density is calculated by subtracting the charge densities of free C and N atoms from the charge density of C$_3$N. The high charge density around N atoms indicate a charge transfer from C to N atoms. The C-N bonds have covalent bond character.

Bader charge was analysis performed with the QUANTUM ESPRESSO code. Our result shows that for C$_3$, each N atom gains about 0.6 electrons from the adjacent C atoms. The charge redistributions are due to the different electro-negativities of the atoms 2.0 (C) and 3.0 (N). First-principles DFT method was used to calculate the STM image which we show in Fig. 1(b). To produce the calculated STM image, the Kohn-Sham charge density was integrated from the Fermi level to 2 eV below the E_F. Inset structure represents C$_3$N repeating unit with carbon atom (gray ball) and nitrogen atom (blue ball).

The electronic band structure, DOS and PDOS of C$_3$N, are shown in Fig. 2(a). The present GGA-PBE calculations demonstrate that C$_3$N is an indirect semiconductor with 0.4 eV band gap between the valence band maximum (VBM) at Γ and the conduction band minimum (CBM) at M point. The energy band gap value can be compared with the measured 2.67 eV by electrochemical method[52] and other experimental (0.39 eV) results.[58] Our calculated gap value using GGA-PBE functional is in good agreement with previous results.[52,57,59] The energy band gap between CB and VB are dominated by the orbital character of C/N-p_z states as shown in Fig. 2(a), with red and green curves near E_F. Since in C$_3$N two C atoms are replaced by N, the p_z orbital band is fully occupied by the additional two electrons. In

addition the higher electro-negativities and smaller atomic size of N as compared with C, result in a shorter partially covalent C-N bond. This leads to semiconducting behavior with band gap between the p_z states forming a Dirac-point, which is 2.25 eV below E_F. The DOS and PDOS of the C_3N, are similar to those of C_3N presented in Fig. 2(a). In addition the density of state (DOS) and Partial DOS were calculated using Gaussian smearing with a width of 0.2 eV. From PDOS, we see that the VBM of C_3N is dominated by the N-p_z orbitals and the Dirac-Point is formed by N-p_z orbitals, whereas the CBM is prominent by C-p_z orbital states. The s-orbital states have a flat band and reflect heavy charge carriers. The C/N-p_z orbitals, open a gap in the C_3N as bonding and antibonding combinations.

The DOS and band structure calculations of pristine C_3N calculated with QUANTUM ESPRESSO (plane-wave basis set)[71] and SIESTA (atomic orbitals basis set),[72] are shown in Fig. 2(b). The unit cell parameters are the same for both cases. The plane-wave basis set takes two orders of magnitude more calculation time as compared to the atomic orbital basis set calculation. One can see from Fig. 2(b), that C_3N VB are identical and it is a semiconductor with an indirect band gap of ~ 0.4 eV using QUANTUM ESPRESSO and SIESTA, and is very similar to the OpenMX results.

Adatoms

Adsorption of adatoms will affect the structural, electronic and magnetic properties of pristine C_3N. The minimum energy or most stable sites of various adsorbed adatoms are obtained by placing the adatom to six prefable adsorption sites at an initiaa height of ~ 2 Å from the surface of C_3N as schematically illustrated in Fig. 3(a). With fully structural optimizations, where all atoms are relaxed in all directions, we determine the most stable site as the minimum energy configuration among the six different sites. These six possible adsorption sites are; (1) the hollow site above the center of a hexagon with six C atoms (H_{CC}), (2) the hollow site above the center of a hexagon composed of both C and N atoms (H_{NC}), (3) the

bridge site above the middle of a C-C bond (B_{CC}), (4) the bridge site above the middle of a N-C bond (B_{NC}), (5) the top site above a C atom (T_C), and (6) the top site above a N atom (T_N) (see Fig. 3(a)). The adsorption energy is defined as $E_a = E_{C_3N} - E_{Ad} - E_{Ad/C_3N}$, where E_{Ad/C_3N} is the total energy of the structure with adatom adsorption on C_3N, E_{C_3N} is total energy of pristine C_3N without adatom, and E_{Ad} is the total energy of an isolated adatom in vacuum. The adatoms adsorption energy, is shown in Fig. 3(b). The variation of structural parameters including bond length, height and buckling for different adatoms adsorbed C_3N at the stable sites, are shown in Figs. 3(c-f).

The structural, electronic and magnetic parameters of Ad/C_3N at the stable adsorption sites involving the T_C, B_{CC} and H_{CC} sites are summarized in Table I. We present also the corresponding structural, electronic and magnetic parameters including bond length between adatom and its nearest atom (d_{AC}); the bond length between C-C atoms (d_{CC}); the bond length between N-C atoms (d_{NC}); the height of adatom from the C_3N plane(h); the buckling of C_3N defined by the difference between the largest and smallest Z coordinates of C atoms in C_3N (Δz); the adsorption energy of adatom, (E_a) and the magnetic moment per supercell (μ). Electronic state is specified as metal (M), half-metal (HM) or semiconductor (SC). The band gap of the system after adsorption (E_g); the charge transfer (ΔQ) between adatoms and C_3N are listed in Table I. The adsorption energy at stable T_C-site, is significantly larger with value in the range $E_a \sim 1.5 - 4.2 eV$ with smaller $d_{AC} \sim$ 1.1-2.4 Å. While at stable B_{CC}-site, B, C, Si, N, P and Cu adatoms, possess adsorption energies in the range $\sim$ 1.8-3.7 eV with smaller $d_{AC} \sim$ 1.4-2.0 Å.

The adsorption energy of Al, AMs (Li, Na and K) and AEMs (Be, Mg and Ca) adatoms at stable H_{CC}-site, in the range of 0.037 eV-0.89 eV and have a larger d_{AC}= 2.2-3.6 Å. For TM adatoms, the adsorption energy is larger than for Al, AM, AEMs and $d_{AC} \sim$ 2-3.5 Å. In the situation that the d_{AC} is long, the E_a tends to decrease and the adatoms show physical adsorption. In contrast, when d_{AC} is short, the E_a tends to increase and the adatom exhibit chemical adsorption. We found that adatom species at stable T_C and B_{CC} sites, causes

the C atom to move out of plane and this geometrical transformation changes the structural parameters. The adsorption of adatom at stable T_C and B_{CC} sites, can result in considerable lattice deformations due to the relative stronger interaction between adatom and C_3N. Thus a buckling of $\Delta z \sim 0.5$ Å of C_3N is occurs; the d_{CC} and d_{NC} with its first neighbors are elongated to ~ 1.50 Å, which compares with 1.40 Å for C_3N.

Now we study the effects of adatoms adsorbed to C_3N at stable T_C-site on electronic and magnetic properties by calculating band structure, DOS and PDOS (see Figs. 4(a,b). Here the analysis of new states appearing around E_F is essential for a better insight of the electronic band structure. We found that the energy band dispersion of pristine C_3N with adsorption of adatom at stable T_C-site is strongly modified by the adatoms. The bonding between adatom and C_3N is covalent. The energy bands below and above E_F are mainly due to the adatom orbital states and appear as localized impurity states. The shape of Dirac-point in pristine C_3N and Ad/C_3N are shown in Fig. 4(a). In comparison with pristine C_3N, the shape of Dirac-point is greatly changed due to the strong disturbance of p_z states caused by the adatom. This illustrates that the interaction between adatom and C_3N may be determined by adatom p_z-orbital states rather than s states. From the DOS and PDOS shown in Fig. 4(b), we can see that the VBM of Ad/C_3N is due to the hybridization of s and $p_{x,y}$-adatoms as well as p_z-orbitals of the nearest C and N atoms. The main contribution to VBM comes from, for example H-s, O-$p_{x,y}$ and C and N-p_z orbitals hybridization, whereas p_z-orbital of O, S adatoms does not mix with surrounding C and N states. The CBM of both O and S is formed by hybridization of $p_{x,y}$ with $p_{x,y,z}$ orbital states of C_3N. The interaction of adatoms with C_3N induces metallic and semiconducting properties. For adatoms at stable T_C-site, the H and Cl/C_3N becomes a metal and the O, S, F/C_3N becomes a semiconductor with $E_g \sim 60$-90 meV. As they mostly provide a p-type charge carrier by moving the E_F to the VB edge. We found that the Ad/C_3N at stable T_C-site exhibits a nonmagnetic ground state (see Table I).

Figs. 5(a,b) show the energy band structure with corresponding DOS and PDOS for

Ad/C_3N (Ad=B, C, Si, N and P). The interaction of these adatoms with C_3N, eliminates the semiconducting band gap of pristine C_3N and induce metallic properties, and mostly provide a p-type charge carrier. From the DOS and PDOS shown in Fig. 5(b), we can see that the VBM of Ad/C_3N is due to the hybridization of $s, p_{x,y,z}$-adatoms orbitals with p_z-orbitals of the nearest C and N atoms. The main contribution to VBM comes from; for example B-s, B-p_z and C and N-p_z orbitals hybridization, whereas B-$p_{x,y}$ and C/N-p_z orbitals does not mix. The CBM of both B and N is formed by hybridization of B-p_x with N-p_z orbital states of C_3N.

Next, we study the adsorption of Al, AMs (Li, Na and K) and AEMs (Be, Mg and Ca) adatoms at stable H_{CC}-site. These adatoms species are located above the hollow site above the center of a hexagon with six C atoms of C_3N at stable H_{CC}-site. In contrast H, O, S, F, C, Si, N and P cause strongly distortions in the C_3N structure, adsorption of Li, Na, K, Be, Mg, Ca and Al adatoms to C_3N, due to the weaker interaction between adatoms and C_3N, does not yield any significant distortion. Accordingly, calculated adsorption energies range between 0.44 and 1.2 eV. The structure of the Ad/C_3N and the structural parameters of the adatoms adsorbed on C_3N are also presented in Fig. 3(e) and Table I. The adatoms adsorbed on C_3N at H_{CC}-site have h=1.8-3.6 Å, and the adatoms do not shift neighboring C atoms and buckling is negligible. Among the adatoms, Na adatom binds most strongly to C_3N, which generates the shortest d_{AC}=2.25 Å and the smallest h=1.83 Å. It is also found that h increases from Li to K due to the increasing atomic radius. The transfer of charge between adatoms and the C_3N is $\sim$ 0.2-0.9 eV for Li, Na and K/C_3N, respectively, indicating an ionic bonding character between adatoms and its neighboring C atoms. The band structure, DOS and PDOS of Ad/C_3N (Ad= Li, Na, K, Be, Mg, Ca and Al) at the stable H_{CC}-site are shown in Figs. 6(a,b). The adsorption of Be, Mg and Ca adatoms turns semiconductor C_3N into metallic. In the case of Be, Mg and Ca, due to the donation of $\sim$ 0.8e charge from the Li, Na and K into C_3N, it remains semiconductor with 0.43, 0.43 and 0.16 eV band gaps, respectively. In comparison with pristine C_3N, the Li, Na and K

adatoms result in bands concentrated mainly at the vicinity of 0.5 eV, which are formed by the hybridization between s-orbital of adatom and C/N-p_z orbital states. Each isolated Li, Na and K has a net initial magnetic moment of 1 μ_B, and the ↑ and ↓ spin degeneracy is not broken upon charge transfer and therefore the Li, Na, K, Be, Mg, Ca and Al/C$_3$N become nonmagnetic.

From the PDOS shown in Fig. 6(b), the VBM of Ad/C$_3$N is due to the hybridization of C-p_z orbital with the Li, Na, K, Be, Mg, Ca and Al adatoms s-orbital states around E_F. Due to the charge transfer, E_F is shifted, while $p_{x,y,z}$-orbital of adatoms does not mix with C states. The CBM of Ad/C$_3$N is due to the hybridization of C-p_z orbital with adatoms $p_{x,y,z}$-orbital states. For example, the CBM of Al is formed by hybridization of Al-p_{xy} and C-p_z orbital states of C$_3$N. Differing from Be and Mg, Ca/C$_3$N yield Ca states around E_F. While the VB originate mainly from the N-p_z orbital states, the CB is composed of C-p_z orbitals.

For the TMs/C$_3$N (TM=Sc, Ti, V, Cr, Mn, Fe, Co, Ni, Cu and Zn), adsorption energies are in the range of ~ 0.08-3 eV (see Table I). Ti and Zn have largest and smallest adsorption energy among TMs adatoms on C$_3$N. The Zn adatom has the largest bond length of 3.4 Å. Top and side views of the structure of TMs/C$_3$N and the structural parameters including d_{AC}, d_{CC}, d_{NC}, h, Δz for adatoms are shown in Fig. 3(f). For TMs/C$_3$N, the adatoms height are also relative larger (about 2-3 Å), while the buckling of C atoms is relative small. For Ti/C$_3$N, a charge accumulation appears in the region between Ti and the neighboring C atoms and shows a strong covalent bonding character in the formed d_{Ti-C}. Such strong covalent bonding is also found in most other TMs/C$_3$N. In addition, we also calculated the charge transfer between TM adatom and the C$_3$N. The corresponding results are listed in Table I, with some degree of ionic bonding for these structures. After optimization, it is the Fe and Co adatoms that bind to the six C with adatom height 1.5 Å for both and d_{Fe-C} and d_{Ni-C} is only 2 Å. We can see that for Cu/C$_3$N at the stable B_{CC}-site, d_{AC}= 2 Å, and the C atoms directly below Cu adatom undergoes a notable displacement towards the opposite

direction, resulting in a buckling of 0.369 Å. However, the charge accumulation in the region between Zn and the neighboring C atoms is less for Zn/C_3N, and thus the d_{Zn-C} only display slightly covalent bonding character.

The band structure of TMs adatoms at stable site with corresponding spin-polarization DOS and PDOS, are shown in Figs. 7(a,b). Though the 3d-orbital have similar energy values with 4s-orbital states, is partially occupied, in addition the initial magnetic moments of isolated TMs are nonzero unless the 3d-orbital shell is completely occupied. As the 3d-orbital are near to the nucleus, TMs with their partially occupied 3d-orbital shells are relaxed to different stable sites on C_3N and we can expect a variety of electronic properties. We can see that in the Sc, Ti and V/C_3N energy bands split into ↑ and ↓ spin channels resulting in a ferromagnetic-metal, while the Cr/C_3N, becomes a direct semiconductor with 0.44 eV band gap. The Mn/C_3N exhibit a ferromagnetic-metal for both ↑ and ↓ spin channels (see Fig. 8(a)). The hybridized sp-orbital states of C and N are shown at the CB and lower energy of the VB (see Fig. 8(b)). For TMs adatoms, strong and weak hybridization between 3d and the C/N-p_z orbital states is found, while we found a strong as well as weak covalent bonding character between TM adatom and C_3N. The TMs adsorption induces magnetic moments in the C_3N yielding an exchange-splitting in 3d-orbital.

In the case of Ni, Cr, Zn and Cu exhibit no spin-splitting due to their nonmagnetic ground state (see Fig. 8(b)). While the isolated Sc, Ti and V adatoms, have initial magnetic moments of 1.0, 2.0 and 3.0 μ_B, respectively and when on C_3N exhibits a ferromagnetic-metal with 1.1, 2.56 and 2.0 μ_B magnetic moments, respectively for the Sc-4s and Sc-3d orbital states, spin-splitting can be found in the vicinity of E_F of the main 3d-orbital peaks located at the CBM zone. Metallic energy bands of the Sc/C_3N originate from the Sc-d_{xy}(↑) and C/N-p_z orbital states. For Ti, the spin-splitting is slightly larger than for Sc, resulting in strong bonding and the degeneracies of the Ti-3d orbital states are broken. Metallic state originate from the $Ti - 3d_{x^2y^2}$(↑)/$4s$(↑) with C and N-p_z(↓) orbital states. In the V/C_3N, metallic energy bands originates from the $3d_{x^2y^2}$(↑)/$4s$(↑) with C-p_z(↓) and N-p_z(↑) orbitals,

respectively. With adsorption of Mn, the degeneracy of ↑ and ↓ spin channels is shifted and induce 3.56 μ_B and both spin states have metallic character, that originates from the $4s(\uparrow)$ and $3d_{z^2}(\downarrow)/3d_{xy}$-orbital at E_F with 3.6 μ_B magnetic moment (see Fig. 7(b)).

The Fe and Co have the smallest atomic size of the considered TMs, they are the most closely bonded one among all TM adatoms. The Fe/C$_3$N, exhibit a dilute-magnetic semi-conductor with an indirect band gap of 0.35 and zero eV in the ↑ and ↓ spin channels, respectively. The bands around E_F mainly originate from the hybridization of Fe-4s(↑) orbital. For Co/C$_3$N, the configuration remains semiconducting with a direct band gap of $\sim$ 0.55 eV in the electron ↑ spin state, whereas the ↓ spin band shows a metallic behavior, thus the density of ↑ and ↓ spin channels exhibit a spin polarization at E_F and Co/C$_3$N becomes a half-metal. This suggests that the charge carriers within the vicinity of E_F are mobile, which is not only useful for conductive behavior but also for magnetic coupling. The bands around E_F mainly originate from the hybridization of $d_{xy,yz,xz}/d_{x^2y^2}(\downarrow)$-orbitals and the C-$p_z(\downarrow)$ orbital states. In addition, the degeneracy of ↑ and ↓ spin states are broken and induces 2.0 and 1.0 μ_B magnetic moments, respectively. Note that the half-metal behavior in Co/C$_3$N can be quite important for application in spintronics. The Ni and Zn/C$_3$N, exhibit a direct semiconductor with 0.46 and 0.4 eV band gaps, respectively, while the Cu/C$_3$N, becomes a metal. For Ni, Zn and Cu/C$_3$N, we can see that the 4s and 3d-orbitals in the ↑ and ↓ spin states are completely occupied and there is no spin-splitting and the configuration is nonmagnetic (see Fig. 8(b)).

In order to know the spin state arrangement on each atom, the difference spin density of the Sc, Ti, V, Mn, Fe and Co/C$_3$N is shown in Fig. 9(a). The blue and yellow colors show the ↑ and ↓ spin states, respectively. The difference spin density of Sc and Ti/C$_3$N, show that the spin accumulates mainly around Sc and Ti adatom with its six C atom neighbors, thus displaying ferromagnetic interaction between them. We can see, a highly localized spin density around V and Mn/C$_3$N and its six C atom neighbors, thus indicating an anti-ferromagnetic interaction between them. The difference spin density of Co/C$_3$N, shows that

the spin accumulates mainly around Co adatom and its six C atom neighbors, thus displaying FM interaction between them, while this is different for Fe/C$_3$N. We can see from right panel of Fig. 9(a), a highly localized difference spin density around Fe adatom and its six C atom neighbors, indicating an anti-ferromagnetic interaction between them.

Adsorption of TMs adatoms on the C$_3$N can significantly modulate the magnetic and electronic properties. In here we analyze the spin-splitting of 3d-orbitals in the TMs/C$_3$N under hexagonal crystal field. The hexagon ring of C$_3$N is made of six C atoms as a stable H_{CC}-site, creating hexagonal crystal field, that can trap TMs adatoms. As a result the occupied asymmetrically $d_{xy}/d_{x^2y^2}$-orbital, could break the hexagonal symmetry leading to a Jahn-Teller-type distortion,[77] which cause TMs adatoms shift toward $d_{xy}/d_{x^2y^2}$ orbitals. From Fig. 9(b), we see that the degenerate 3d-orbitals are broken into three energy levels, which consist of two-fold degenerate d_{xz}/d_{yz} and $d_{x^2y^2}/d_{xy}$ with non-degenerate d_{z^2}-orbital. Due to the repulsive effect between 3d-orbital electrons and the C-$p_{x,y}$ orbital states, the in-plane 3d-orbitals including $d_{xy}/d_{x^2y^2}$-orbitals, have a relatively higher energy because of facing the C-$p_{x,y}$ orbitals, while the other orbitals are out of plane, such as d_{xz}, d_{yz} and d_{z^2}-orbitals that are located at lower energy.

In order to reveal whether the adatoms adsorbed on C$_3$N can diffuse or migrate, we investigate as an example the energy barriers for the displacement of single H, O and F adatoms. The variation of total energy in the Ad/C$_3$N at the symmetry points and motion along the $T_C \longrightarrow B_{CC} \longrightarrow H_{CC} \longrightarrow T_C$ directions or the migration on a hexagon is shown in Fig. 10. By using these total energy curves we obtain the energy barriers that have to be overcome by the adsorbate in order to diffuse or migrate on the C$_3$N surface. The minimum energy barrier occurs at the B_{CC}-site between two adjacent T_C-sites. This analysis suggests that a diffusing adatom can take a path of minimum energy barrier following the edges of the hexagon at one T_C-site to an other T_C-site through the barrier in the range of 1-4 eV at H_{CC}-site. This barrier energy is very large and does not allow adatoms to migrate on the surface of C$_3$N.

Effect of charging, electric field and strain

We present here the effect of charging, electric field and strain on the properties of C_3N. In Figs. 11(a,b), the changes in the band structure and DOS with charging are shown. For q = +1 e, the Fermi level shift into the VBM and creates holes, while for q = -1 e, the Fermi level shifts into the CBM and creates electrons. Incidentally, as a result of negative charging (q = -8 e), Dirac-point moves to the Fermi level and the VBM and CBM touch each other at the Fermi level. The electronic band structure and DOS of the C_3N as a function of electric field, is shown in Fig. 11(c). The F= +0.1 and -0.1 V/Å denotes electric field parallel and antiparallel to the z-axis, respectively. For both F = +0.1 and -0.1 V/Å, the C_3N did not yield any change in electronic state as a result of applied electrical field.

The 2DM are often put on a substrate which may induce strain. Strain engineering is an important method to change the properties of 2DM. We investigate the effects of uniaxial and biaxial strains in the tensile and compression states on the C_3N monolayer. The tensile and compression strain are defined as $\varepsilon = (\frac{a \pm a_0}{a_0}) \times 100$, where a and a_0 are strained and non-strained lattice constants, respectively. The positive and negative values denotes tensile and compression states, respectively. The uniaxial and biaxial strains are applied along zigzag and ab-axis direction, respectively. The band structure under uniaxial strain in tensile and compression state, are shown in Figs. 12(a,b). Under uniaxial tensile strain along zigzag direction, C_3N exhibit a metallic character when it is larger than +14%. The reason is that the CBM at the K point shifts down and in the VBM vicinity the Γ point rises up to E_F. Interestingly, the Dirac-point (located at about -2.25 eV) will move away from the K point to the M point. Under uniaxial compression strain along zigzag direction the structure becomes metallic when larger than -8% and the Dirac-point will move away from the K point to the M point. The band structure under biaxial strains are shown in Figs. 12(c,d). For biaxial compression strain, we can see from Fig. 12(c) that C_3N transforms into a metal if the amount of compression strain is larger than -8%. This differs from the case of biaxial tensile strain where semiconducting behavior is found up to +14%. Fig. 12(e), shows the variation

of energy band gap with strain. The energy band with increase of uniaxial strain, decreases to zero gap for compression strain of -8%, and becomes metallic for tensile strain of +14%. In addition, the band gap increases from 0.4 eV as biaxial tensile strain is applied to C_3N and the energy band gap increases with biaxial compression and becomes metal at -8%.

The effect of charging, electric field and strain on the electronic and magnetic properties of the Ti, Mn and Fe/C_3N are here discussed. We show the calculated variation of the magnetic moment with charging in the case of q = +1 e (when one electron is removed) and q = -1 e (when one electron is added). The variations of the calculated magnetic moment of the Ti, Mn and Fe/C_3N as a function of charging, is shown in the lower insets of Fig. 13(a). Our results show that the Ti/C_3N becomes spin-polarized with 2.58 μ_B and the magnetic moment increases to 2.6 μ_B at q = +1 e and remains a ferromagnetic-metal, whereas for excess electronic charge of q = -1 e, the magnetic moment increases to 2.95 μ_B and it become a ferromagnetic-half metal (see Fig. 13(b)). Namely it is metal for one spin channel, but a semiconductor for the opposite spin channel. This material transports electrons only in one spin channel and can function as a spin valve. The Mn/C_3N is a ferromagnetic-metal with 3.47 μ_B and reach 2.62 μ_B, when 1 electron is removed (q = +1 e) from the Mn/C_3N and it remains metal. Under excess electronic charge a reverse situation is observed, where the magnetic moment decreases to 4 μ_B for q = -1 e and C_3N becomes a semiconductor. For Fe/C_3N, which is a semiconductor with 2 μ_B in neutral state, magnetic moment decreases to 0.11 μ_B (at q = +1 e) and 1.51 μ_B (at q = -1 e) and becomes metal. The variation of magnetic moment is due to the accommodation of different electronic charges of TMs 3d -orbital states for different values of q.

The variation of magnetic moment for Ti, Mn and Fe adatoms as a function of electric field is now investigated (see Figs. 14(a,b)). F= +0.1 and -0.1 V/Å which denotes electric field parallel and antiparallel to the z-axis, respectively. The applied electric field effects on the electronic and magnetic properties are significant and cause spin polarizations of Ti, Mn and Fe/C_3N. In the case of Ti/C_3N, magnetic moments decreases to 2.37 μ_B with F = +0.1

V/Å, and increases to 2.74 μ_B for F= -0.1 V/Å. In both cases it remains a metal. For F = +0.1 V/Å, the charge on the Ti decreases with increasing F and Ti/C_3N remains metal and with F = -0.1 V/Å, the charge of Ti enhances with increasing of F and excess electronic charge on the Ti adatom is transferred from C atoms. The magnetic moment of Mn/C_3N decreases to 3.33 μ_B (at F = +0.1 V/Å), and increases to 3.62 μ_B (at F = -0.1 V/Å).

Now, the strain effect on the electronic and magnetic properties of the TMs/C_3N are investigated. The band structure under uniaxial tensile and compression strain for Mn and Fe/C_3N are shown in Figs. 15(a,b). The range of uniaxial strain is from -8% to $+8\%$. We see, that Mn/C_3N is initially a ferromagnetic-metal but becomes half-metal under compression larger than -8%, while with increasing tensile strain, the structure preserves ferromagnetic-metallic character. The Fe/C_3N is a dilute-magnetic semiconductor, and we can see that C_3N transforms into a half-metal if the amount of compression strain is larger than -8%, while Fe/C_3N, keeps its dilute-magnetic semiconducting character with increasing strain to +8% (see Fig. 15(b)). Fig. 15(c) shows the variation of the energy band gap of Fe/C_3N with strain. The band gap decreases with increase of uniaxial strain and becomes zero for compression, and remains semiconductor with increasing tensile strain but the band gap decreases for both ↑ and ↓ spin channels. The variation of magnetic moment of Mn and Fe/C_3N as a function of uniaxial strain, is shown in Fig. 15(d). For Mn/C_3N, magnetic moment decreases from 3.5 μ_B to 3 μ_B with tensile strain of +8%, and increases to larger than 3.7 μ_B with increasing compression strain. The magnetic moment of Fe/C_3N is approximately constant in the range of -8% to $+8\%$. For Ti/C_3N the magnetic moment is approximately constant in the range of 0% to -8% and decreases in the range of 0% to $+8\%$.

Adatom coverage dependence

The electronic properties of C_3N strongly depend on the adatom coverage and the exact pattern of coverage. As an example we consider the electronic structure corresponding to H and B atoms adsorbed at different stable T_C-sites of the C_3N with 1H/1B (3.1%), 2H/2B (6.2%), 3H/3B (9.3%) and 4H/4B (12.5%) adatom coverages per computational unit cell (see Figs. 16(a,b)). We found that H and B coverage alter the atomic structure of C_3N as compared with that of pristine C_3N. In the case of 1H and 1B/C_3N (3.1%), nearest C atom moves in the upward direction. As the H and B adsorbed ratio increases to two (7.14%), the surface distortion becomes more apparent and the bond length is changed significantly. With further increase of H and B coverage, a similar behavior is observed with more distorted surface geometry. Our results show that the H and B adatoms adsorption cause a strong structural distortion and this may result in a modification of the electronic structure. The 1H and 1B/C_3N, displays a metallic behavior unlike pristine C_3N. As the H and B coverage increases to 7.14%, metallic behavior increasingly appears and we found a metallic state. Further increase of H coverage to 9.3% and 12.5%, we still obtain metallic behavior. Our results shows that the electronic structure of C_3N is significantly affected by H and B atoms coverages.

In the following, we investigate the structural and electronic properties of the semi and full coverage of C_3N with H atom in chair-like conformation. Hereafter, the semi-hydrogenated C_3N and fully-hydrogenated C_3N, will be labeled with SH and FH-C_3N abbreviations, respectively. The optimized structures and corresponding structural parameters such as lattice constant, the bond lengths between C-H, N-C and C-C and buckling parameter for semi and fully hydrogenated-C_3N, are shown in Figs. 17(a,c). For C_3N, the lattice constant and the bond length between C-H, N-C and C-C are slightly enhanced upon semi and fully hydrogenation. My results show that H atom are adsorbed on C atom with bonds arranged approximately normal to the C_3N surface. In general, the C-C ad C-N bond lengths without hydrognation is smaller than that between the C and N atoms with one or both C and N

atoms bonded with H atoms (C-C_H or C_H-C_H). Notice that SH- and FH-C$_3$N have slightly enlarges lattice constant from 4.861 in pristine C$_3$N, to 5.080 and 5.313 Å, respectively. The increase in the lattice parameter is due to the increase in the bond length, which is increased from 1.4 to 1.5 (for SH-C$_3$N) and 1.6 Å (for FH-C$_3$N). For chair-like SH-C$_3$N, C_HH bond length is 1.147 Å and bond angle between C_H-N-C_H, N-C_H-C and C-C_HC are 105, 113 and 115°, respectively. The values of buckling for SH and FH-C$_3$N are 0.114 Å and 0.244 Å, respectively. The difference charge density are shown in Figs. 17(a,c), with high charge density around C and N atoms. The high charge density around C bonded to H and N atoms projected toward the C-N and C-H bonds indicate charge transfer from C to N and H atoms.

In order to understand the effects of SH, SF-C$_3$N, we investigate the energy band structures, DOS and PDOS. The electronic structure with corresponding DOS and PDOS of semi and fully hydrogenated-C$_3$N are shown in Figs. 17(b,d). Our result shows that SH-C$_3$N is metallic, while FH-C$_3$N is an insulator with 4.8 eV band gap. From DOS and PDOS in Figs. 17(b,d), we can see that the metallic behavior, mainly comes from the H and N atomic orbitals. The band gap in FH-C$_3$N comes from the C-p_z orbital which lowers in energy and the nature of hydrogenation determines the lowering. In SH-C$_3$N, all the H atoms are held at one side, which naturally results in a repulsion among the H atoms that results in a shift of most C-p_z orbital type band. This further causes the crystal to expand. It becomes evident from comparison that in case of FH-C$_3$N, the C-p_z and H-s orbitals are shifted toward E_F. In fact, the contribution from C-p_z orbital is almost as large as that of H-s orbital. The difference charge density are presented in the lower insets of Figs. 17(a,c). Notice, there is a charge accumulation in the region between the H atom and the neighboring C atoms, resulting in a strong H-C covalent bond. The electronic structure of C$_3$N is modified by adsorption of two H on two-sided of C$_3$N. We found that the energy band dispersion is strongly disturbed, thus the bonding type between H and C$_3$N is covalent.

The optimized atomic structures, band structures and DOS for adsorption of two H atoms

on two-sided C_3N are shown in Fig. 18(a). After relaxation, the C-C_H-N bond angle is 110°. The bond length between H and its C atoms is 1.118 Å. We see from Fig. 18(a), that the C atoms directly below H atom undergoes a notable shifting towards the opposite direction, thus finally resulting in buckling of 0.650 Å. The interaction of 2H on two-sided C_3N, induce metallic property and shows a nonmagnetic ground state.

Vacancy

Next, we consider one H atom vacancy (1H-vacancy) from single-sided FH-C_3N. The optimized atomic structure of 1H-vacancy in FH-C_3N is shown in Fig. 18(b). Each 1H-vacancy can be created by removing H atoms from single side, leading to a half-filled sp^3-like orbital on the C_3N surface whereas the band gap decrease by the vacancy defect states that are located around E_F. Here it is worth to note that each 1H-vacancy induce a local magnetic moment of 1 μ_B, as shown in Fig. 18(b). Upon desorption of a single H atom, local bonding through sp^3 bonding orbital is re-transformed into planar sp^3 bonding and perpendicular p_z-orbitals. At the vacancy site one electron accommodated by the dangling p_z-orbital becomes unpaired and hence induce a 1 μ_B magnetic moment. We can see from Fig. 18(b), that FH-C_3N becomes an insulator with 4.8 eV band gap and attains permanent magnetic moment in the presence of 1H-vacancy. The magnetic properties with magnetic moments on C_3N are useful for future data storage and spintronics applications.

Summary and conclusions

In summary, based on first-principles calculations, we investigated the structural, electronic and magnetic properties of a novel 2D material, with stoichiometry C_3N that has been recently synthesized from carbonized organic single crystals. The C_3N is an indirect band-gap semiconductor. This study highlights that the adatom adsorption to C_3N is a favorable approach to modulate its properties which may have significant importance because of its

basic relevance to applications in catalysis, batteries and nanoelectronics. These results will be very useful for theoretical and experimental studies that are considering the use of atoms and molecules as building blocks for making new nano devices. We investigated systematically the interaction between 27 different adatoms and the C_3N honeycomb structure. These adatoms lead to considerable modifications in the electronic structure, when the related adsorption energy is significant. Under these conditions, the band gap of C_3N can be reduced and the system becomes metal or semiconductor. We presented here the effect of charging, electric field and strain on the electronic and magnetic properties of C_3N and Ti, Mn and Fe/C_3N. Our results show that the band gap and magnetic moment considerable changes with charging, applied electric field and strain. In this way it is possible to tune the electronic and magnetic properties.

We predict that C_3N can withstand a strain of $+19$, $+15\%$ for uniaxial strain along zigzag or armchair directions, and $+15\%$ for biaxial strain along ab-axis. It is found that C_3N is destroyed through the breaking of the C-N bonds, which suggests that C-C bonds in C_3N are stronger than the C-N bonds.

From pristine C_3N with semi-hydrogenated and then to fully-hydrogenated, C_3N changes from semiconductor to metal and then to insulator. The functionalization provides a novel approach to tune the properties of C_3N. Our calculations show that adsorption of adatoms on C_3N provides viable electronic and magnetic properties which can be useful in a diversity of future applications including, solar cells, photocatalysis, sensors, nanoelectronics and nano-magnetics devices. Moreover the existence of a tunable band gap in C_3N is highly desirable for its use in nanoscale optoelectronic device applications.

Acknowledgment

References

(1) Novoselov, K. S.; Geim, A. K.; Morozov, S. V.; Jiang, D.; Zhang, Y.; Dubonos, S. V.; Grigorieva, I. V.; Firsov, A. A. Electric Field Effect in Atomically Thin Carbon Films. *Science* **2004**, *306*, 666–669.

(2) Castro Neto, A. H.; Guinea, F.; Peres, N. M. R.; Novoselov, K. S.; Geim, A. K. The Electronic Properties of Graphene. *Rev. Mod. Phys.* **2009**, *81*, 109–162.

(3) Novoselov, K. S.; Jiang, D.; Schedin, F.; Booth, T. J.; Khotkevich, V. V.; Morozov, S. V.; Geim, A. K. Two-Dimensional Atomic Crystals. *Proceedings of the National Academy of Sciences* **2005**, *102*, 10451–10453.

(4) Li, Y.; Zhou, Z.; Yu, G.; Chen, W.; Chen, Z. CO Catalytic Oxidation on Iron-Embedded Graphene: Computational Quest for Low-Cost Nanocatalysts. *J. Phys. Chem. C.* **2010**, *114*, 6250–6254.

(5) Balandin, A. A.; Ghosh, S.; Bao, W.; Calizo, I.; Teweldebrhan, D.; Miao, F.; Lau, C. N. Superior Thermal Conductivity of Single-Layer Graphene. *Nano Lett.* **2008**, *8*, 902–907.

(6) Geim, A. K.; Novoselov, K. S. The Rise of Graphene. *Nat. Mater.* **2007**, *63*, 183–91.

(7) Kaukonen, M.; Krasheninnikov, A. V.; Kauppinen, E.; Nieminen, R. M. Doped Graphene as a Material for Oxygen Reduction Reaction in Hydrogen Fuel Cells: A Computational Study. *ACS Catal.* **2013**, *3*, 159–165.

(8) Cabria, I.; López, M. J.; Alonso, J. A. Enhancement of Hydrogen Physisorption on Graphene and Carbon Nanotubes by Li Doping. *J. Chem. Phys.* **2005**, *123*, 204721.

(9) Pumera, M. Graphene-Based Nanomaterials for Energy Storage. *Energy Environ. Sci.* **2011**, *4*, 668–674.

(10) López-Corral, I.; Germán, E.; Juan, A.; Volpe, M. A.; Brizuela, G. P. DFT Study of Hydrogen Adsorption on Palladium Decorated Graphene. *J. Phys. Chem. C.* **2011**, *115*, 4315–4323.

(11) Lin, Y.-M.; Dimitrakopoulos, C.; Jenkins, K. A.; Farmer, D. B.; Chiu, H.-Y.; Grill, A.; Avouris, P. 100-GHz Transistors from Wafer-Scale Epitaxial Graphene. *Science* **2010**, *327*, 662–662.

(12) Cheng, R.; Bai, J.; Liao, L.; Zhou, H.; Chen, Y.; Liu, L.; Lin, Y.-C.; Jiang, S.; Huang, Y.; Duan, X. High-Frequency Self-Aligned Graphene Transistors with Transferred Gate Stacks. *Proceedings of the National Academy of Sciences* **2012**, *109*, 11588–11592.

(13) Son, Y.-W.; Cohen, M. L.; Louie, S. G. Half-Metallic Graphene Nanoribbons. *Nature* **2006**, *444*, 347.

(14) Yazyev, O. V.; Katsnelson, M. I. Magnetic Correlations at Graphene Edges: Basis for Novel Spintronics Devices. *Phys. Rev. Lett.* **2008**, *100*, 047209.

(15) Schedin, F.; Geim, A. K.; Morozov, S. V.; Hill, E. W.; Blake, P.; Katsnelson, M. I.; Novoselov, K. S. Detection of Individual Gas Molecules Adsorbed on Graphene. *Nat. Mater.* **2007**, *6*, 652–655.

(16) Schwierz, F. Graphene Transistors. *Nat. Nano.* **2010**, *5*, 487–496.

(17) Han, M. Y.; Özyilmaz, B.; Zhang, Y.; Kim, P. Energy Band-Gap Engineering of Graphene Nanoribbons. *Phys. Rev. Lett.* **2007**, *98*, 206805.

(18) Li, X.; Wang, X.; Zhang, L.; Lee, S.; Dai, H. Chemically Derived, Ultrasmooth Graphene Nanoribbon Semiconductors. *Science* **2008**, *319*, 1229–1232.

(19) Giovannetti, G.; Khomyakov, P. A.; Brocks, G.; Kelly, P. J.; van den Brink, J.

Substrate-Induced Band Gap in Graphene on Hexagonal Boron Nitride: Ab Initio Density Functional Calculations. *Phys. Rev. B* **2007**, *76*, 073103.

(20) Balog, R.; Jrgensen, B.; Nilsson, L.; Andersen, M.; Rienks, E.; Bianchi, M.; Fanetti, M.; Lgsgaard, E.; Baraldi, A.; Lizzit, S.; Sljivancanin, Z.; Besenbacher, F.; Hammer, B.; Pedersen, T. G. Bandgap Opening in Graphene Induced by Patterned Hydrogen Adsorption. *Nat. Mater.* **2010**, *9*, 315.

(21) Haberer, D.; Vyalikh, D. V.; Taioli, S.; Dora, B.; Farjam, M.; Fink, J.; Marchenko, D.; Pichler, T.; Ziegler, K.; Simonucci, S.; Dresselhaus, M. S.; Knupfer, M.; Büchner, B.; Grüneis, A. Tunable Band Gap in Hydrogenated Quasi-Free-Standing Graphene. *Nano Lett.* **2010**, *10*, 3360–3366.

(22) Haberer, D.; Petaccia, L.; Farjam, M.; Taioli, S.; Jafari, S. A.; Nefedov, A.; Zhang, W.; Calliari, L.; Scarduelli, G.; Dora, B.; Vyalikh, D. V.; Pichler, T.; Woll, C.; Alfe, D.; Simonucci, S. Direct Observation of a Dispersionless Impurity Band in Hydrogenated Graphene. *Phys. Rev. B* **2011**, *83*, 165433.

(23) Yazyev, O. V. Emergence of Magnetism in Graphene Materials and Nanostructures. *Reports on Progress in Physics* **2010**, *73*, 056501.

(24) Ponomarenko, Z. H., Ni; Nair, L. A.; Yang, R. R.; Anissimova, R.; Grigorieva, S.; Schedin, I. V.; Blake, F.; Shen, P.; Hill, Z. X.; H., E.; Novoselov, K. S.; Geim, A. K. On Resonant Scatterers As a Factor Limiting Carrier Mobility in Graphene. *Nano Lett.* **2010**, *10*, 3868–3872.

(25) Katoch, J.; Chen, J.-H.; Tsuchikawa, R.; Smith, C. W.; Mucciolo, E. R.; Ishigami, M. Uncovering the Dominant Scatterer in Graphene Sheets on SiO_2. *Phys. Rev. B* **2010**, *82*, 081417.

(26) Chan, K. T.; Neaton, J. B.; Cohen, M. L. First-Principles Study of Metal Adatom Adsorption on Graphene. *Phys. Rev. B* **2008**, *77*, 235430.

(27) Sahin, H.; Peeters, F. M. Adsorption of Alkali, Alkaline-Earth, and 3d Transition Metal Atoms on Silicene. *Phys. Rev. B* **2013**, *87*, 085423.

(28) Pang, Q.; Li, L.; Zhang, L.-L.; Zhang, C.; Song, Y.-L. Functionalization of Germanene by Metal Atoms Adsorption: A First-Principles Study. *Can. J. Phys.* **2015**, *93*, 1310–1318.

(29) Kadioglu, Y.; Ersan, F.; Gökolu, G.; Üzengi Aktürk, O.; Aktürk, E. Adsorption of Alkali and Alkaline-Earth Metal Atoms on Stanene: A First-Principles Study. *Mater. Chem. Phys.* **2016**, *180*, 326–331.

(30) Li, Y.; Xia, C.; Du, J.; Xiong, W.; Li, X.; Wei, S. Influences of the Adsorption of Different Elements on the Electronic Structures of a Tin Sulfide Monolayer. *Phys. Chem. Chem. Phys.* **2017**, *19*, 5423–5429.

(31) Lalitha, M.; Mahadevan, S. S.; Lakshmipathi, S. Improved Lithium Adsorption in Boron- and Nitrogen-Substituted Graphene Derivatives. *J. Mater. Sci.* **2017**, *52*, 815–831.

(32) Roldan, R.; Chirolli, L.; Prada, E.; Silva-Guillen, J. A.; San-Jose, P.; Guinea, F. Theory of 2D Crystals: Graphene and Beyond. *Chem. Soc. Rev.* **2017**, *46*, 4387–4399.

(33) Lee, C.; Wei, X.; Kysar, J. W.; Hone, J. Measurement of the Elastic Properties and Intrinsic Strength of Monolayer Graphene. *Science* **2008**, *321*, 385–388.

(34) Geim, A. K.; Grigorieva, I. V. Van der Waals Heterostructures. *Nature* **2013**, *499*, 419–425.

(35) Resta, A.; Leoni, T.; Barth, C.; Ranguis, A.; Becker, C.; Bruhn, T.; Vogt, P.; Le Lay, G. Atomic Structures of Silicene Layers Grown on Ag(111): Scanning Tunneling Microscopy and Noncontact Atomic Force Microscopy Observations. *Sci. Rep.* **2013**, *3*, 2399.

(36) Gao, J.; Zhang, G.; Zhang, Y.-W. Exploring Ag(111) Substrate for Epitaxially Growing Monolayer Stanene: A First-Principles Study. *Sci. Rep.* **2016**, *6*, 29107.

(37) Xu, Y.; Yan, B.; Zhang, H.-J.; Wang, J.; Xu, G.; Tang, P.; Duan, W.; Zhang, S.-C. Large-Gap Quantum Spin Hall Insulators in Tin Films. *Phys. Rev. Lett.* **2013**, *111*, 136804.

(38) Molle, A.; Goldberger, J.; Houssa, M.; Xu, Y.; Zhang, S.-C.; Akinwande, D. Buckled Two-Dimensional MXene sheets. *Nat. Mater.* **2017**, *16*, 163.

(39) Wu, D.; Wang, Y.; Wang, F.; Wang, H.; An, Y.; Gao, Z.; Xu, F.; Jiang, K. Oxygen-Incorporated Few-Layer MoS_2 Vertically Aligned on Three-Dimensional Graphene Matrix for Enhanced Catalytic Performances in Quantum Dot Sensitized Solar Cells. *Carbon* **2017**, *123*, 756 – 766.

(40) Long, L.-L.; Zhang, A.-Y.; Huang, Y.-X.; Zhang, X.; Yu, H.-Q. A Robust Cocatalyst Pd_4S Uniformly Anchored onto Bi_2S_3 Nanorods for Enhanced Visible Light Photocatalysis. *J. Mater. Chem. A* **2015**, *3*, 4301–4306.

(41) Tang, Q.; Zhou, Z.; Shen, P. Are MXenes Promising Anode Materials for Li Ion Batteries? Computational Studies on Electronic Properties and Li Storage Capability of Ti_3C_2 and $Ti_3C_2X_2$ (X = F, OH) Monolayer. *J. Am. Chem. Soc.* **2012**, *134*, 16909–16916.

(42) Jun, Y.; E., R. C.; Kathleen, M.; B., H. C.; Babak, A.; Patrick, U.; Asya, S.; Yury, G. Flexible MXene/Graphene Films for Ultrafast Supercapacitors with Outstanding Volumetric Capacitance. *Adv. Func. Mater.* **2014**, *27*, 1701264.

(43) Wen, Y.; Rufford, T. E.; Chen, X.; Li, N.; Lyu, M.; Dai, L.; Wang, L. Nitrogen-Doped Ti_3C_2Tx MXene Electrodes for High-Performance Supercapacitors. *Nano Energy* **2017**, *38*, 368 – 376.

(44) Xiong, W.; Xia, C.; Wang, T.; Du, J.; Peng, Y.; Zhao, X.; Jia, Y. Tuning Electronic Structures of the Stanene Monolayer via Defects and Transition-Metal-Embedding: Spin-Orbit Coupling. *Phys. Chem. Chem. Phys.* **2016**, *18*, 28759–28766.

(45) Chintalapati, S.; Shen, L.; Xiong, Q.; Feng, Y. P. Magnetism in Phosphorene: Interplay Between Vacancy and Strain. *Appl. Phys. Lett.* **2015**, *107*, 072401.

(46) Gao, D.; Shi, S.; Tao, K.; Xia, B.; Xue, D. Tunable Ferromagnetic Ordering in MoS_2 Nanosheets with Fluorine Adsorption. *Nanoscale* **2015**, *7*, 4211 – 4216.

(47) Ramasubramaniam, A.; Naveh, D. Mn-Doped Monolayer MoS_2: An Atomically Thin Dilute Magnetic Semiconductor. *Phys. Rev. B* **2013**, *87*, 195201.

(48) Ding, Y.; Wang, Y. Structural, Electronic, and Magnetic Properties of Adatom Adsorptions on Black and Blue Phosphorene: A First-Principles Study. *Phys. Chem. Chem. Phys.* **2015**, *119*, 10610 – 10622.

(49) Naqvi, S. R.; Hussain, T.; Luo, W.; Ahuja, R. Exploring Doping Characteristics of Various Adatoms on Single-layer Stanene. *Phys. Chem. Chem. Phys.* **2017**, *121*, 7667 7676.

(50) Peyghan, A. A.; Moradi, M. DFT Study of Ozone Dissociation on BC_3 Graphene with Stone–Wales Defects. *J. Molecular Model.* **2014**, *20*, 2071.

(51) Peyghan, A. A.; Noei, M. Fluorination of BC_3 Danotubes: DFT Dtudies. *J. Molecular Model.* **2013**, *19*, 3941–3946.

(52) Mahmood, J.; Lee, E. K.; Jung, M.; Shin, D.; Choi, H.-J.; Seo, J.-M.; Jung, S.-M.; Kim, D.; Li, F.; Lah, M. S.; Park, N.; Shin, H.-J.; Oh, J. H.; Baek, J.-B. Two-Dimensional Polyaniline (C_3N) from Carbonized Organic Single Crystals in Solid State. *Proceedings of the National Academy of Sciences* **2016**, *113*, 7414–7419.

(53) Chang, M.-Y.; Wu, C.-S.; Chen, Y.-F.; Hsieh, B.-Z.; Huang, W.-Y.; Ho, K.-S.; Hsieh, T.-H.; Han, Y.-K. Polymer Solar Cells Incorporating One-Dimensional Polyaniline Nanotubes. *Organic Electronic.* **2008**, *9*, 1136 – 1139.

(54) Alam, M. M.; Wang, J.; Guo, Y.; Lee, S. P.; Tseng, H.-R. Electrolyte-Gated Transistors Based on Conducting Polymer Nanowire Junction Arrays. *J. Phys. Chem. B* **2005**, *109*, 12777–12784.

(55) Jiantie, X.; Javeed, M.; Yuhai, D.; Shixue, D.; Feng, L.; Liming, D.; Beom, B. J. 2D Frameworks of C_2N and C_3N as New Anode Materials for LithiumIon Batteries. *Adv. Mater. 29*, 1702007.

(56) Mizuno, S.; Fujita, M.; Nakao, K. Electronic States of Graphitic Heterocompounds of Carbon, Boron and Nitrogen. *Synthetic Metals* **1995**, *71*, 1869 – 1870.

(57) Qianku, H.; Qinghua, W.; Haiyan, W.; Julong, H.; Guanglei, Z. First-Principles Studies of Structural and Electronic Properties of Layered C_3N Phases. *physica status solidi (b)* **2011**, *249*, 784–788.

(58) Siwei, Y.; Wei, L.; Caichao, Y.; Gang, W.; He, T.; Chong, Z.; Peng, H.; Guqiao, D.; Xiaoming, X.; Yang, L.; Yeshayahu, L.; ShuitTong, L.; Zhenhui, K.; Mianheng, J. C_3N–A 2D Crystalline, Hole Free, Tunable Narrow Bandgap Semiconductor with Ferromagnetic Properties. *Adv. Mater.* **2016**, *29*, 1605625.

(59) Xiang, H. J.; Huang, B.; Li, Z. Y.; Wei, S.-H.; Yang, J. L.; Gong, X. G. Ordered Semiconducting Nitrogen-Graphene Alloys. *Phys. Rev. X* **2012**, *2*, 011003.

(60) Mortazavi, B. Ultra High Stiffness and Thermal Conductivity of Graphene Like C_3N. *Carbon* **2017**, *118*, 25 – 34.

(61) Makaremi, M.; Mortazavi, B.; Singh, C. V. Adsorption of Metallic, Metalloidic, and

Nonmetallic Adatoms on Two-Dimensional C$_3$N. *J. Phys. Chem. C.* **2017**, *121*, 18575 – 18583.

(62) Pashangpour, M.; Peyghan, A. A. Adsorption of Carbon Monoxide on the Pristine, B- and Al-Doped C$_3$N Nanosheets. *J. Molecular Model.* **2015**, *21*, 116.

(63) Tagani, M. B. Electrical and Mechanical Properties of a Fully Hydrogenated Two-Dimensional Polyaniline Sheet. *Comput. Mater. Sci.* **2018**, *153*, 126 – 133.

(64) Tagani, M. B.; Vishkayi, S. I. Polyaniline (C$_3$N) Nanoribbons: Magnetic Metal, Semi-conductor, and Half-Metal. *J. Appl. Phys.* **2018**, *124*, 084304.

(65) Ozaki, T. Variationally Optimized Atomic Orbitals for Large-Scale Electronic Structures. *Phys. Rev. B* **2003**, *67*, 155108.

(66) Ozaki, T.; Kino, H. Numerical Atomic Basis Orbitals from H to Kr. *Phys. Rev. B* **2004**, *69*, 195113.

(67) Perdew, J. P.; Burke, K.; Ernzerhof, M. Generalized Gradient Approximation Made Simple. *Phys. Rev. Lett.* **1996**, *77*, 3865–3868.

(68) Troullier, N.; Martins, J. L. Efficient Pseudopotentials for Plane-Wave Calculations. *Phys. Rev. B* **1991**, *43*, 1993–2006.

(69) Monkhorst, H. J.; Pack, J. D. Special Points for Brillouin-Zone Integrations. *Phys. Rev. B* **1976**, *13*, 5188–5192.

(70) Mulliken, R. S. Electronic Population Analysis on LCAOMO Molecular Wave Functions. IV. Bonding and Antibonding in LCAO and Valence Bond Theories. *J. Chem. Phys.* **1955**, *23*, 2343–2346.

(71) Giannozzi, P.; Baroni, S.; Bonini, N.; Calandra, M.; Car, R.; Cavazzoni, C.; Ceresoli, D.; Chiarotti, G. L.; Cococcioni, M.; Dabo, I.; Dal Corso, A.; de Gironcoli, S.; et al.,

QUANTUM ESPRESSO: A Modular and Open-Source Software Project for Quantum Simulations of Materials. *J. Phys.: Condens. Matter* **2009**, *21*, 395502.

(72) Soler, J. M.; Artacho, E.; Gale, J. D.; García, A.; Junquera, J.; Ordejón, P.; Sánchez-Portal, D. The SIESTA Method for ab Initio Order-N Materials Simulation. *J. Phys.: Condens. Matter* **2002**, *14*, 2745.

(73) Buko, T.; Hafner, J.; Lebègue, S.; Ángyán, J. G. Improved Description of the Structure of Molecular and Layered Crystals: Ab Initio DFT Calculations with van der Waals Corrections. *J. Phys. Chem. A* **2010**, *114*, 11814–11824.

(74) Jónsson, H.; Mills, G.; Jacobsen, K. W. Nudged Elastic Band Method for Finding Minimum Energy Paths of Transitions. *World Scientific* **1998**, 385–404.

(75) Tersoff, J.; Hamann, D. R. Theory and Application for the Scanning Tunneling Microscope. *Phys. Rev. Lett.* **1983**, *50*, 1998–2001.

(76) Horcas, I.; Fernández, R.; Gómez-Rodríguez, J. M.; Colchero, J.; Gómez-Herrero, J.; Baro, A. M. WSxM: A Software for Scanning Probe Microscopy and a Tool for Nanotechnology. *Rev. Sci. Inst.* **2007**, *78*, 013705.

(77) Jahn, H. A.; Teller, E. Stability of Polyatomic Molecules in Degenerate Electronic States - I—Orbital Degeneracy. *Proc. Royal Soc. London A: Mathematical, Physical and Engineering Sciences* **1937**, *161*, 220–235.

Table 1: The structural, electronic and magnetic parameters of Ad/C_3N at the stable adsorption sites T_C, B_{CC} and H_{CC} shown in Fig. 3(a). The corresponding structural, electronic and magnetic parameters including bond length between adatom and its nearest atom (d_{AC}); the bond length between C-C atoms (d_{CC}); the bond length between N-C atoms (d_{NC}); the height of adatom from the C_3N plane(h); the buckling of C_3N defined by the difference between the largest and smallest z coordinates of C atoms in C_3N (Δz); the adsorption energy of adatom, (E_a); the magnetic moment per supercell (μ). Electronic states are specified as metal (M), half-metal (HM) or semiconductor (SC). The band gap the system after adsorption (E_g); the charge transfer (ΔQ) between adatoms and C_3N are also listed.

| adatom	Site	E_a (eV)	d_{AC} (Å)	h (Å)	d_{NC} (Å)	d_{CC} (Å)	Δz (Å)	ΔQ (e)	$M_{tot}(\mu_B)$	E_g (eV)
H	T_C	1.891	1.121	1.597	1.503	1.495	0.509	0.02	0	M
O	T_C	4.22	1.305	1.937	1.569	1.522	0.640	-1.98	0	M
S	T_C	2.654	1.809	2.322	1.506	1.496	0.517	-0.73	0	M
F	T_C	3.297	1.530	1.948	1.452	1.469	0.439	-0.95	0	M
Cl	T_C	1.685	2.485	2.559	1.410	1.422	0.083	-0.37	0	M
B	B_{CC}	1.846	1.644	1.904	1.460	1.537	0.464	-1.15	0	M
C	B_{CC}	3.756	1.522	1.781	1.444	1.522	0.469	+0.23	0	M
Si	B_{CC}	2.054	2.006	2.339	1.470	1.498	0.479	+1.13	0	M
N	B_{CC}	3.575	1.430	1.690	1.497	1.461	0.469	-1.24	0	M
P	B_{CC}	1.836	1.895	2.230	1.481	1.491	0.493	+1.46	0	M
Li	H_{CC}	0.837	2.254	1.834	1.396	1.417	0.059	+0.95	0	M
Na	H_{CC}	0.89	2.927	2.597	1.400	1.409	0.031	+0.88	0	M
K	H_{CC}	0.71	3.074	2.737	1.401	1.409	0.004	+0.74	0	M
Be	H_{CC}	0.44	3.476	3.153	1.403	1.402	-0.027	+0.01	0	SC(0.43)
Mg	H_{CC}	0.037	3.650	3.309	1.404	1.402	-0.061	+0.23	0	SC(0.43)
Ca	H_{CC}	0.44	2.774	2.384	1.402	1.385	-0.008	+0.92	0	M
Al	H_{CC}	1.219	2.596	2.227	1.391	1.391	0.052	+1.34	0	SC(0.16)
Sc	H_{CC}	1.551	2.297	1.961	1.418	1.442	0.156	+1.12	1.10	M
Ti	H_{CC}	3.137	2.267	1.778	1.403	1.415	0.007	+0.98	2.56	M
V	H_{CC}	2.136	2.159	1.627	1.407	1.412	-0.005	+0.99	1.97	M
Cr	H_{CC}	1.201	2.074	1.459	1.408	1.416	-0.093	+0.76	0.00	SC(0.44)
Mn	H_{CC}	1.714	2.092	1.599	1.405	1.413	0.058	+0.55	3.50	M
Fe	H_{CC}	2.647	2.042	1.489	1.406	1.417	0.020	+0.73	2.00	SC(0.35)
Co	H_{CC}	2.790	2.050	1.485	1.406	1.419	0.008	+0.64	1	HM
Ni	H_{CC}	1.808	2.090	1.616	1.407	1.422	0.085	+0.59	0.00	SC(0.46)
Cu	B_{CC}	0.457	2.082	2.450	1.449	1.457	0.369	+0.05	0.09	M
Zn	H_{CC}	0.079	3.427	3.085	1.404	1.402	-0.042	+0.03	0.00	SC(0.4)
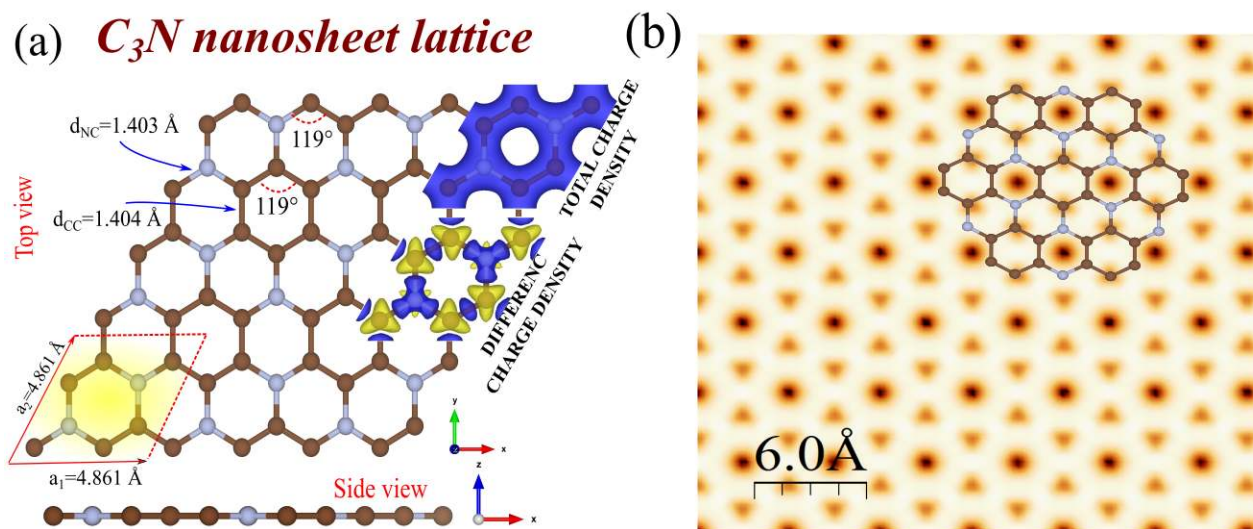
Figure 1: (a) The optimized atomic structure of C_3N, with its hexagonal primitive unit cell, indicated by a red parallelogram. The blue (brown) dots are N (C) atoms. The total and difference charge density isosurfaces are also shown in the same panel. (b) Simulated STM image of C_3N structure. Inset structure represents C_3N repeating unit cell.
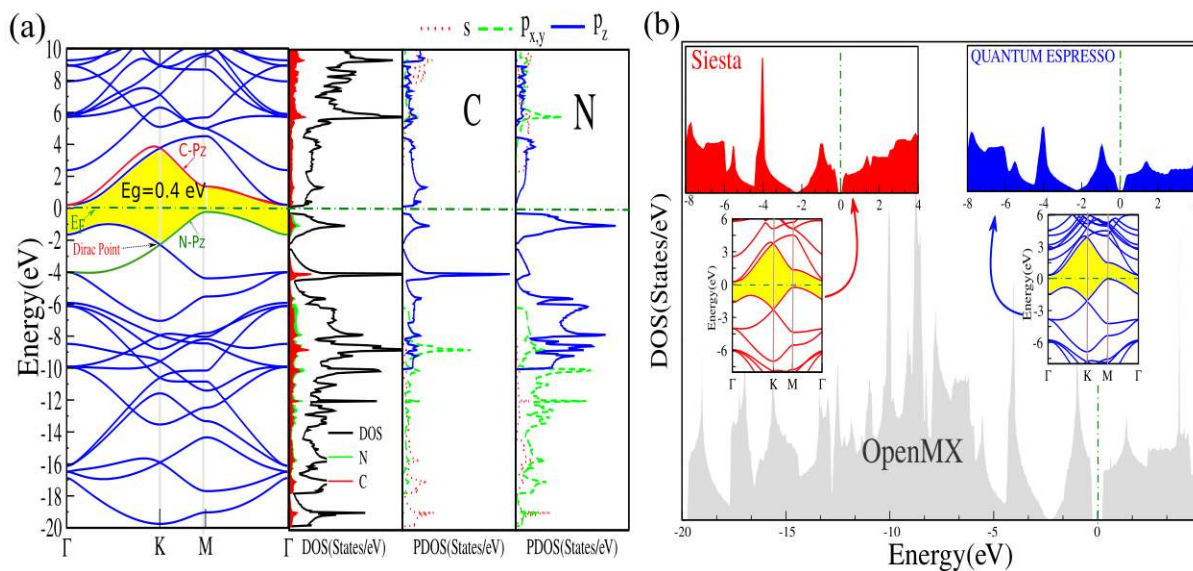
Figure 2: (a) Electronic band structure of C_3N with corresponding DOS and PDOS on C and N atoms. The zero of energy is set to the Fermi level (E_F). (b) The DOS and band structure (insets) of C_3N calculated with OpenMX, QUANTUM ESPRESSO and SIESTA codes.
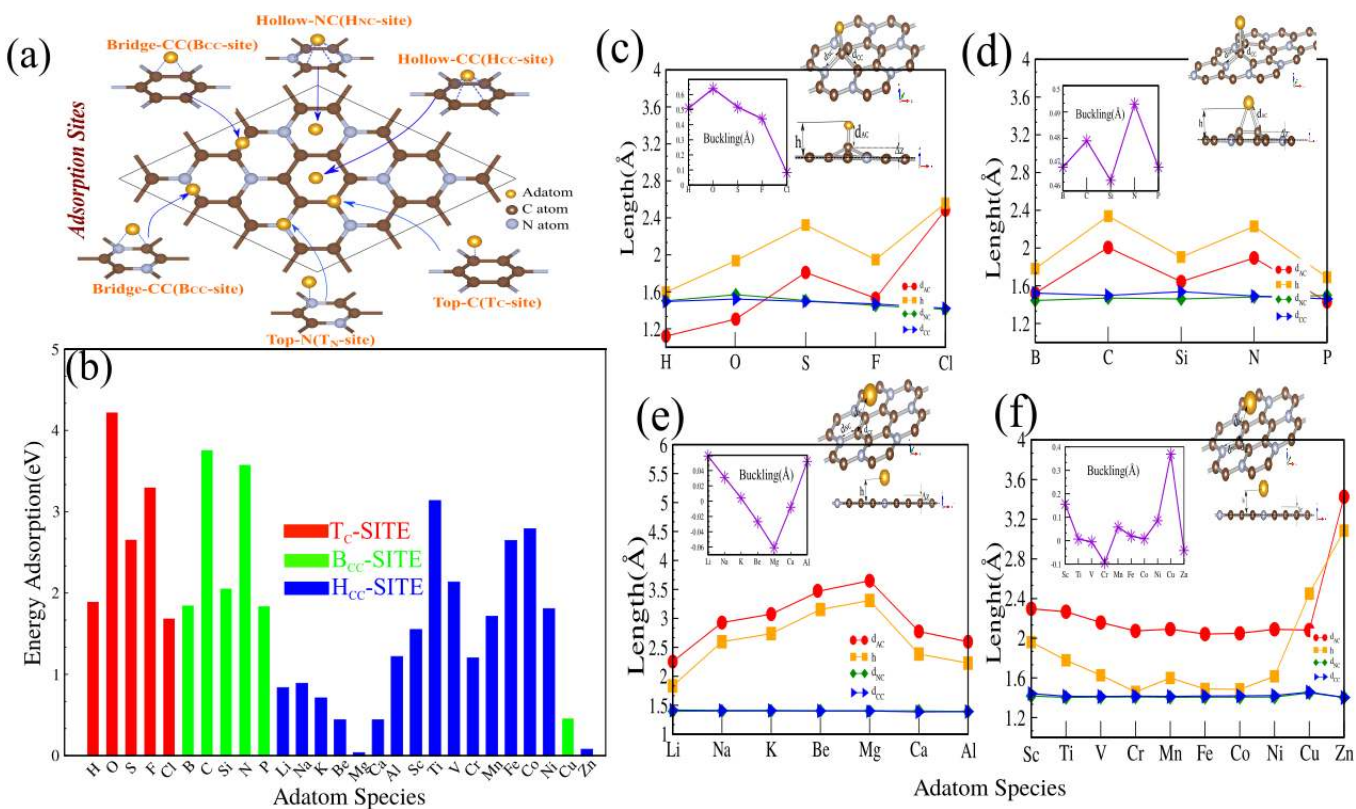
Figure 3: (a) Schematic view of possible adsorption sites of adatoms on C₃N. (b) Adsorption energy of different atoms on C₃N. (c-f) Variation of structural parameters including bond lengths, height and buckling for different adatoms adsorbed on C₃N at the stable sites.
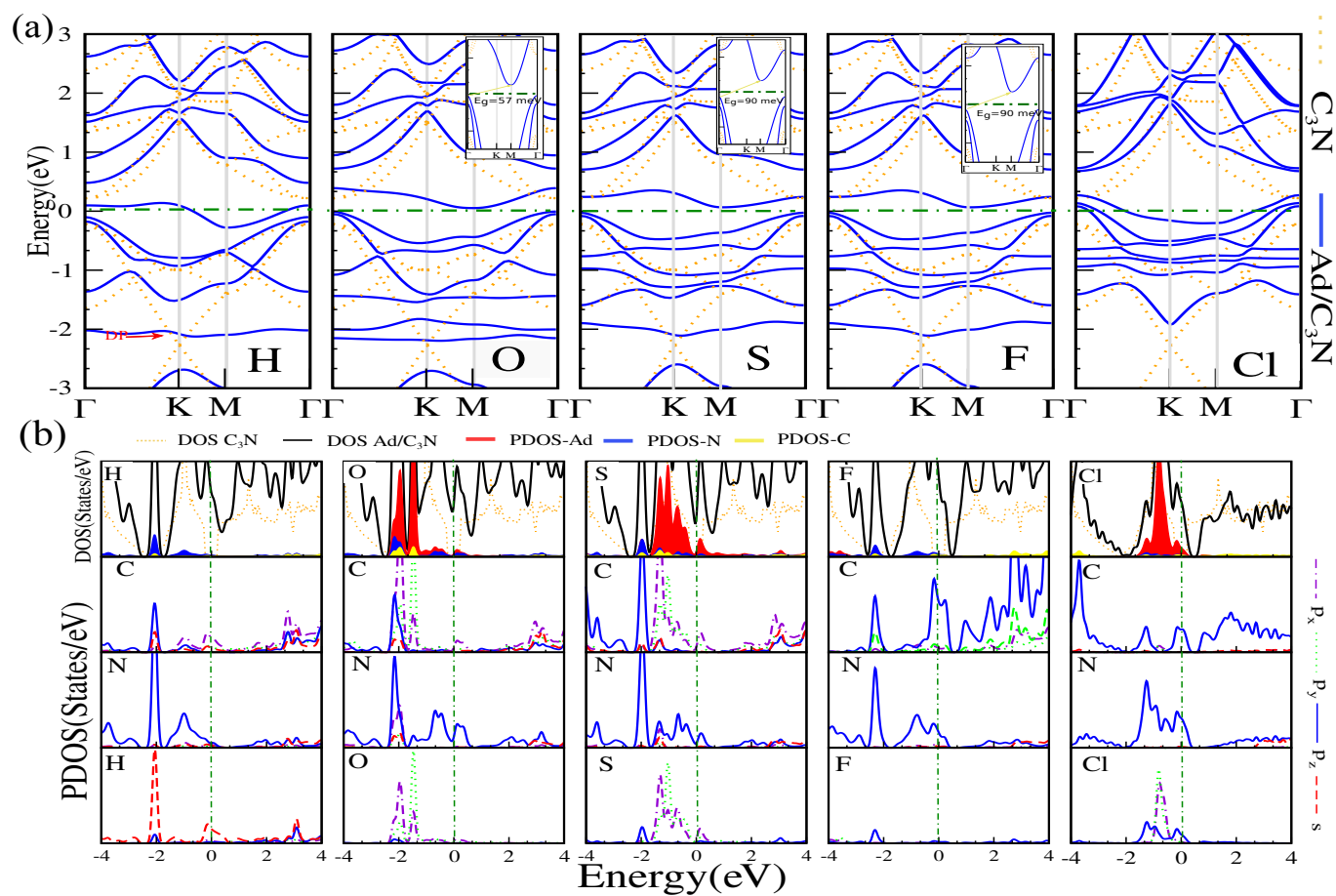
Figure 4: (a) Electronic band structure with corresponding (b) DOS and PDOS of C_3N with H, O, S, F and Cl adatoms at stable T_C-site. The zero of energy is set to E_F, shown by the green dash-point line.
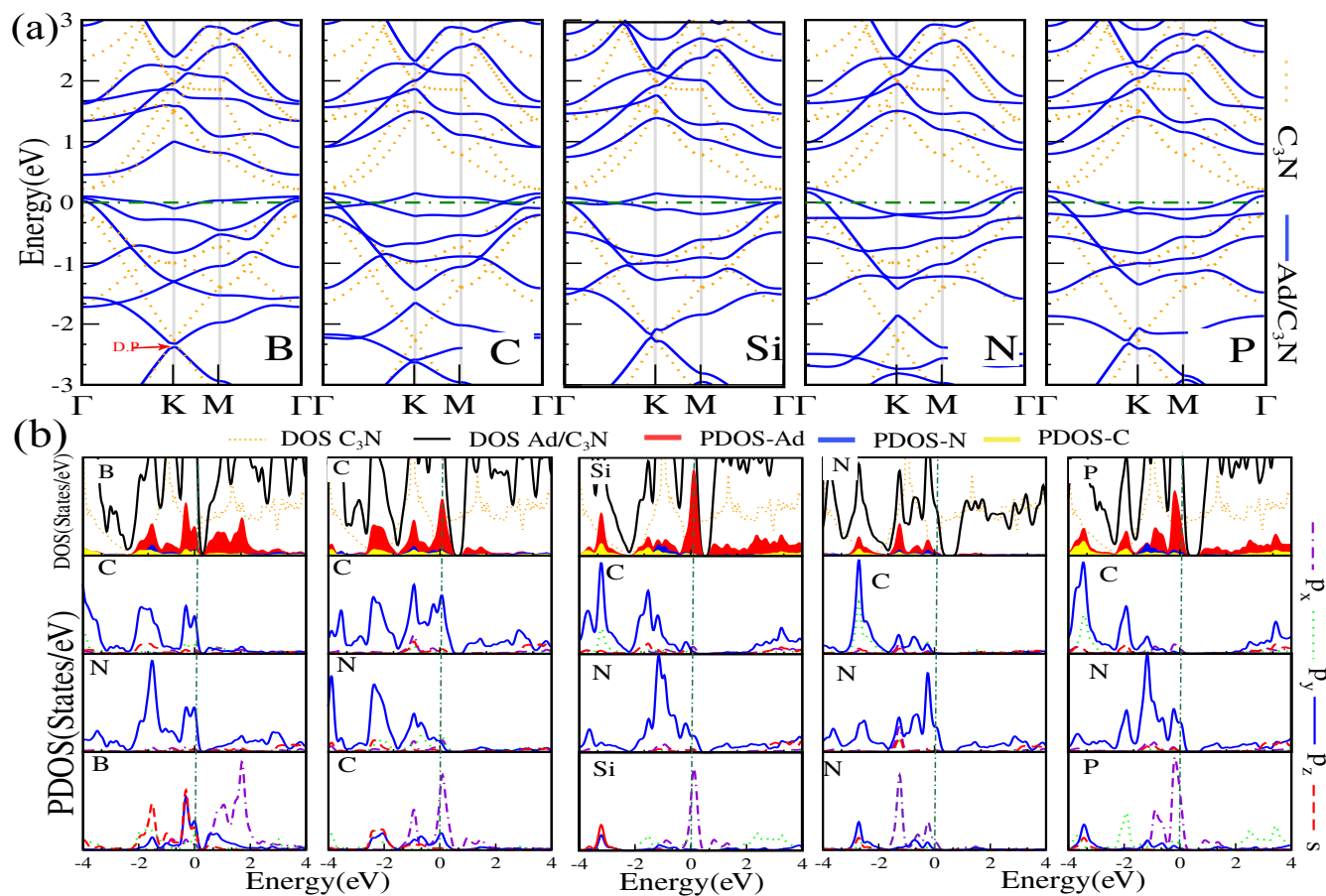
Figure 5: (a) Electronic band structure with corresponding (b) DOS and PDOS of adsorbed B, C, Si, N and P adatoms at T_C-site. The zero of energy is set to E_F, shown by the green dash-point line.
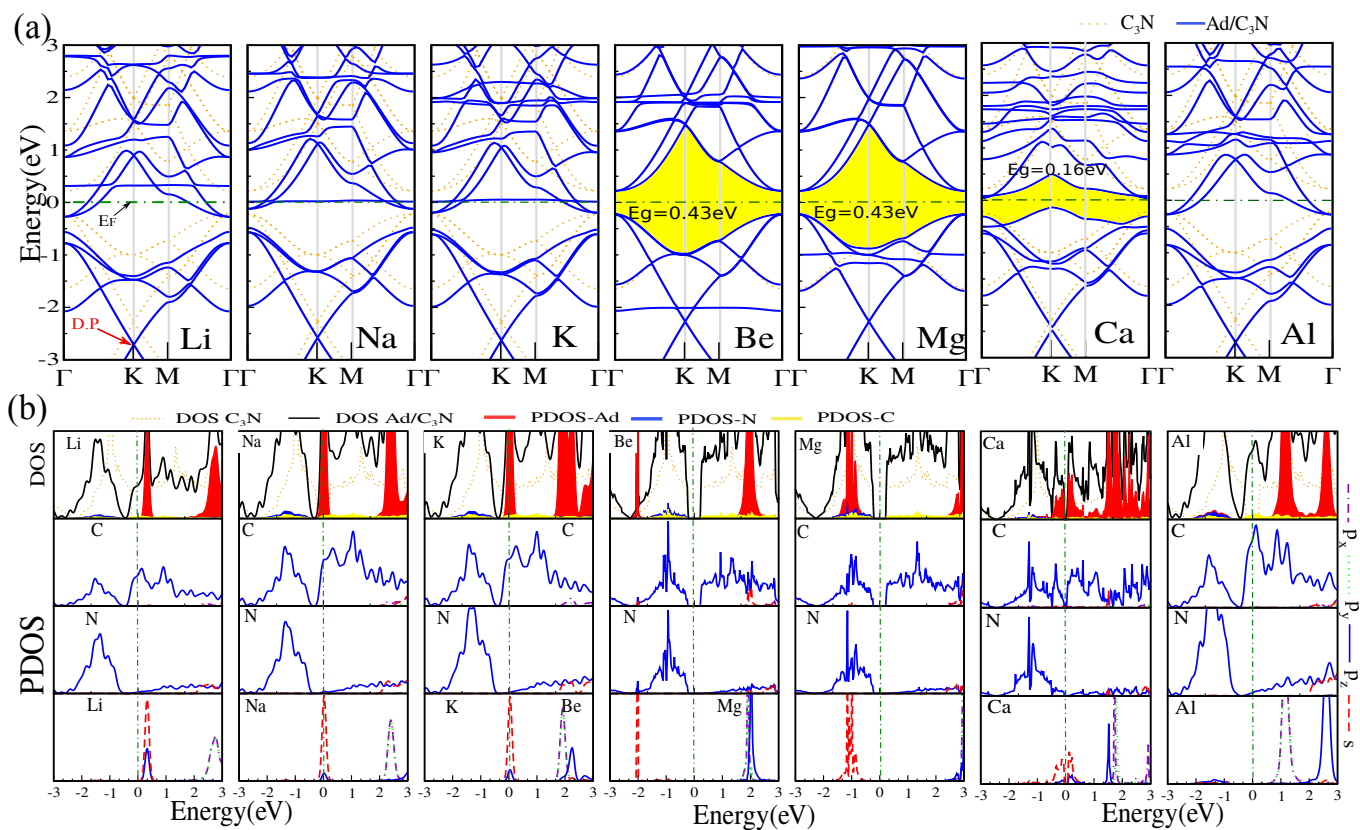
Figure 6: (a) Electronic band structure with corresponding (b) DOS and PDOS of adsorbed Li, Na, K, Be, Mg, Ca and Al adatoms at stable H_{CC}-site. The zero of energy is set to E_F shown by the green dash-point line.
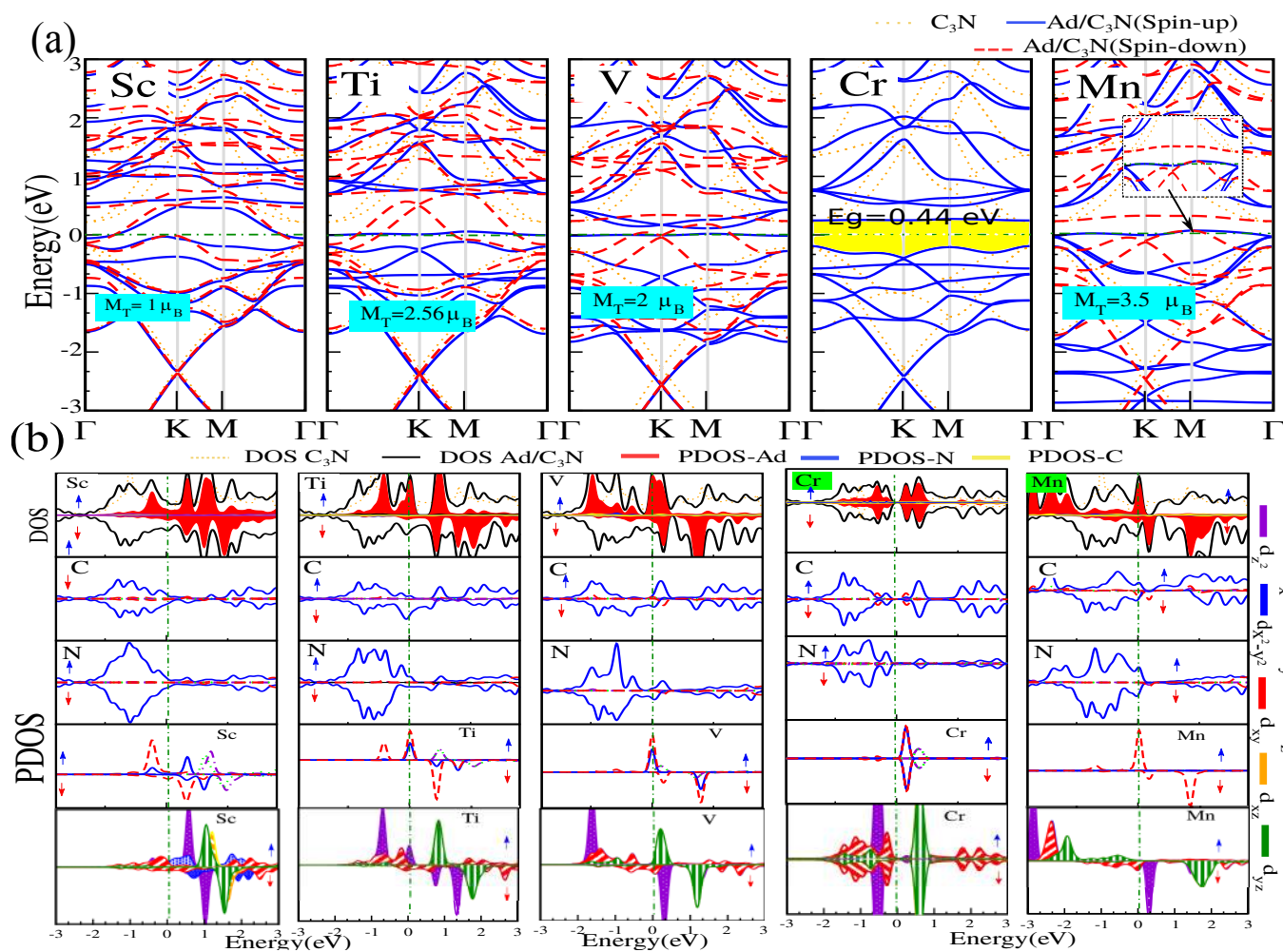
Figure 7: (a) Electronic band structure with corresponding (b) DOS and PDOS of adsorbed Sc, Ti, V, Cr and Mn adatoms at stable H_{CC}-site. The zero of energy is set to E_F, shown by the green dash-point line.
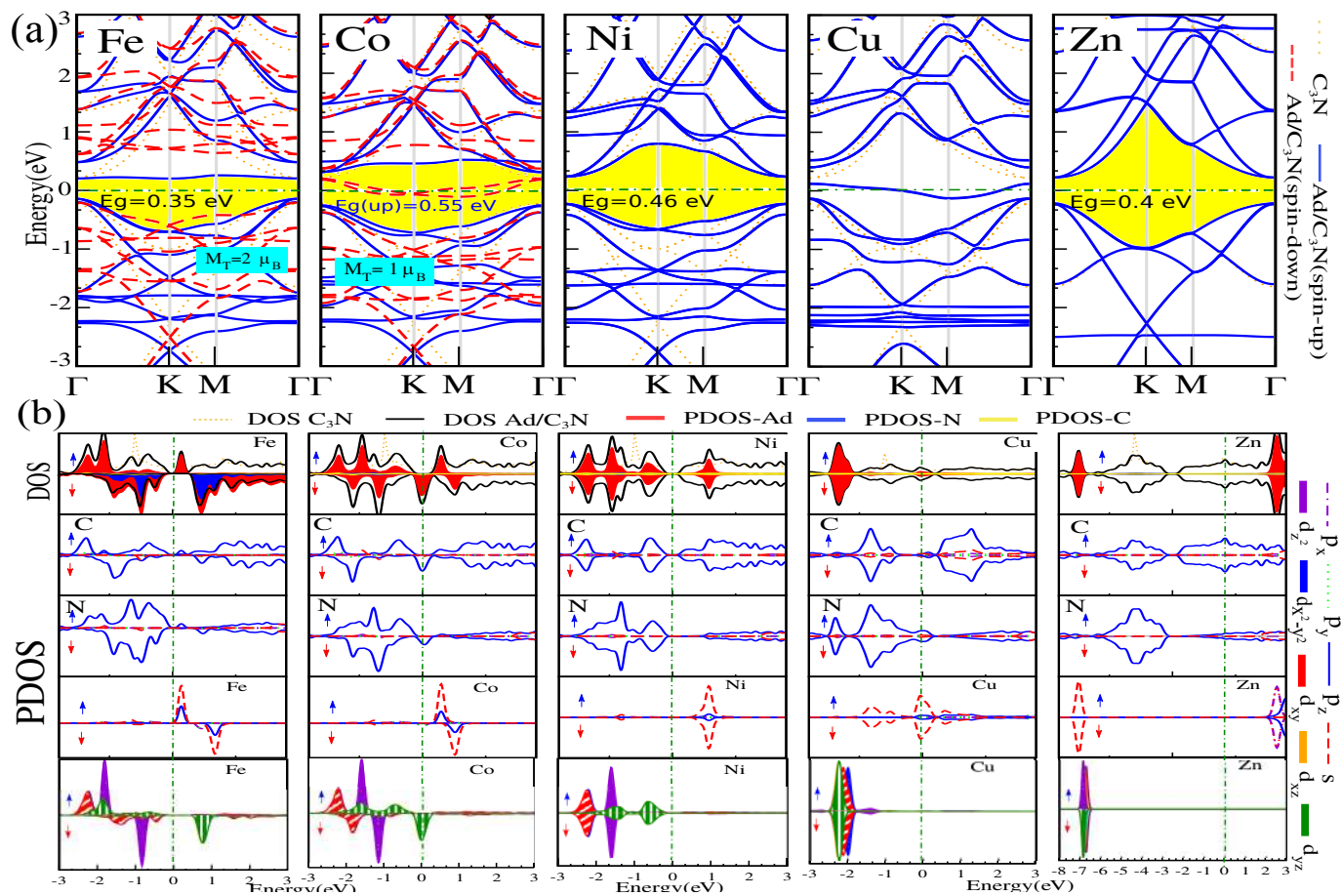
Figure 8: (a) Electronic band structure with corresponding (b) DOS and PDOS of adsorbed Fe, Co, Ni, Cu and Zn adatoms at stable site. The zero of energy is set to E_F, shown by the green dash-point line.
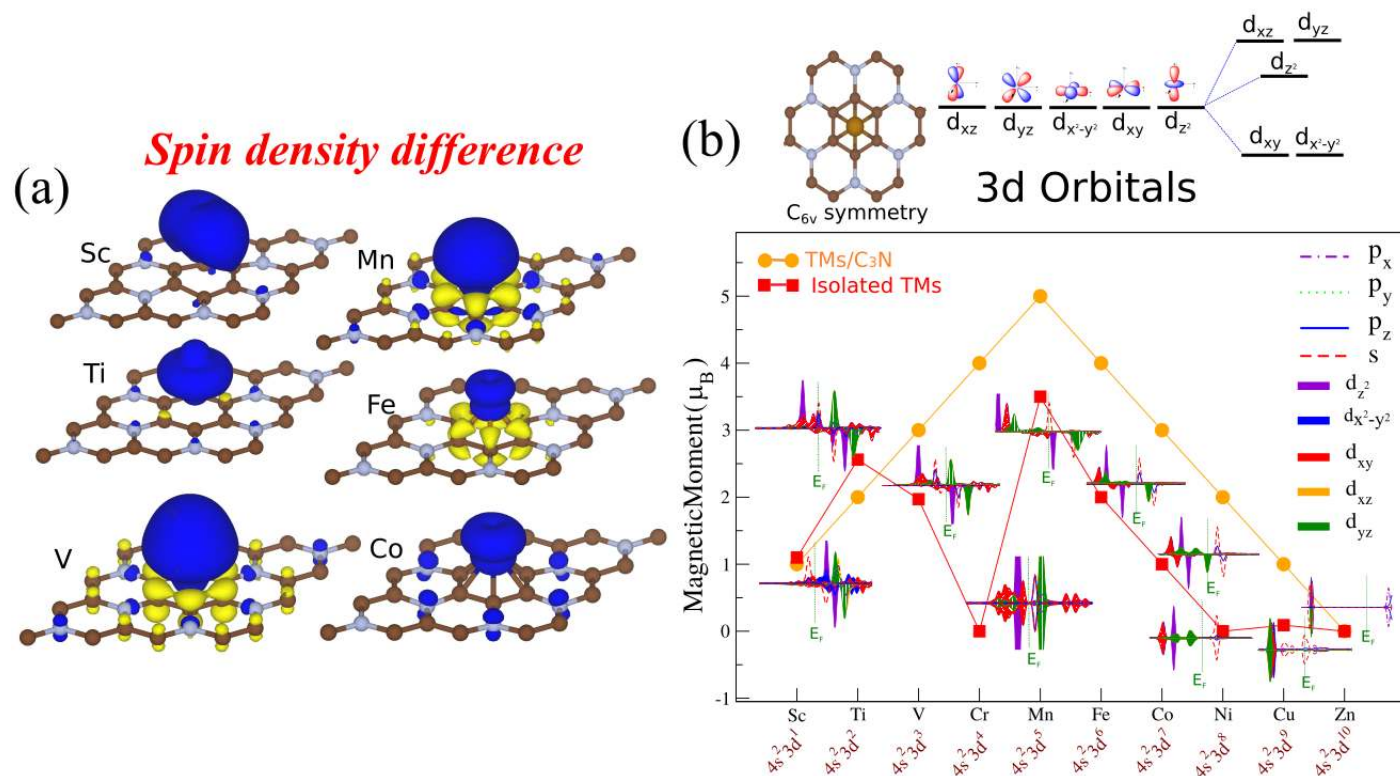
Figure 9: (a) Difference spin density of the Ad/C$_3$N (Ad= Sc, Ti, V, Mn, Fe and Co). The blue and yellow colors show the ↑ and ↓ spin states, respectively. (b) Magnetic moment of Ad/C$_3$N. The energy scheme of 3d-orbital spin-splitting under hexagonal crystal field (top figure).
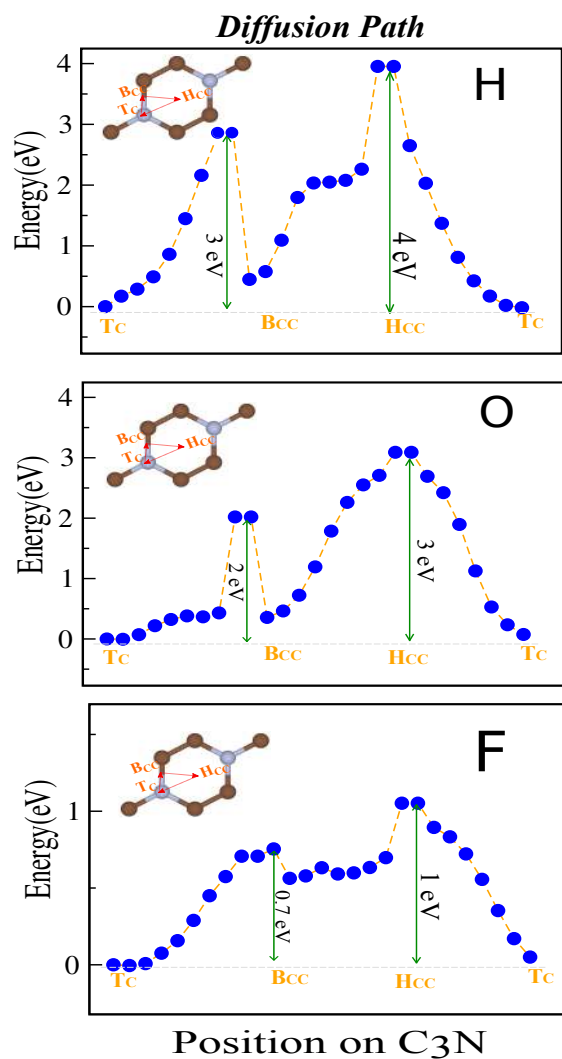
Figure 10: Variation of total energy in the H, O and F adsorbed C_3N at the symmetry points and motion along the $T_C \longrightarrow B_{CC} \longrightarrow H_{CC} \longrightarrow T_C$ directions as shown in the insets.
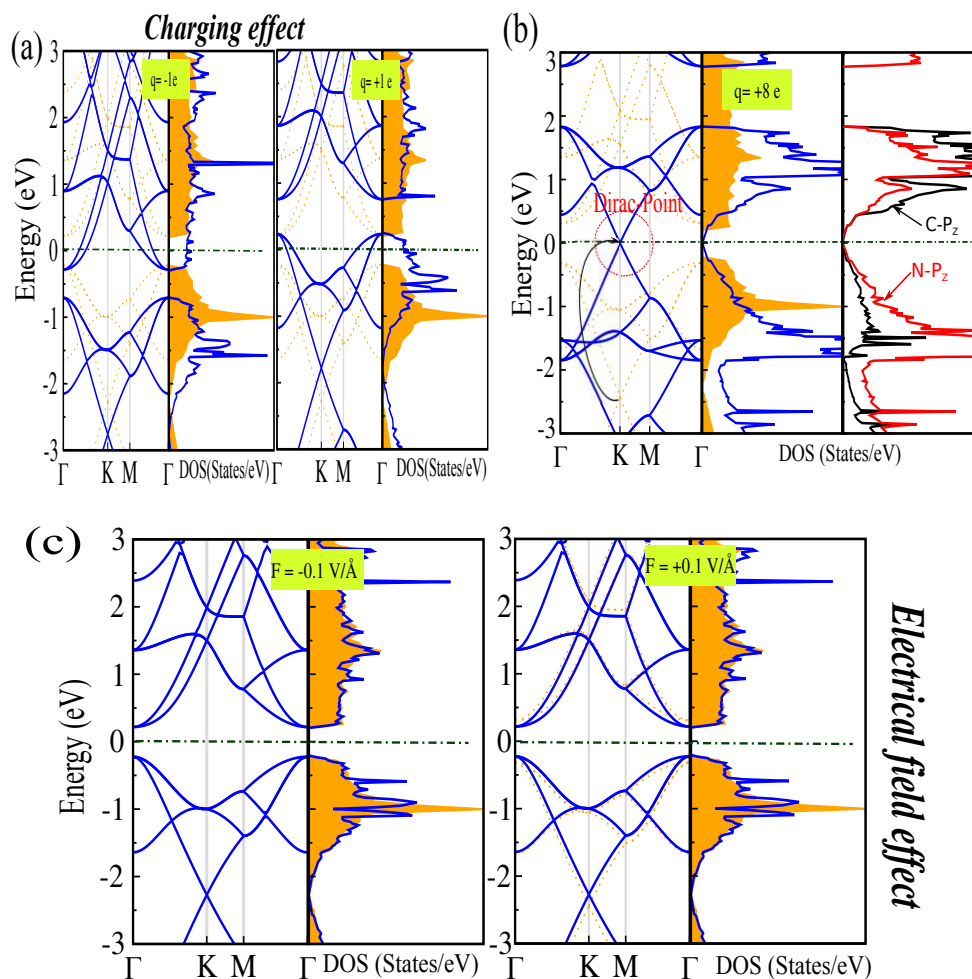
Figure 11: Electronic band structure and DOS of C$_3$N as a function of (a,b) charging and (c) electric field. The q= +1 e and q= -1 e, corresponds to charging where one electron is removed from and added to the C$_3$N, respectively. The F= +0.1 and -0.1 V/Å denotes parallel and antiparallel to the z-axis, respectively. The zero of energy is set to E_F, shown by the green dash-point line.
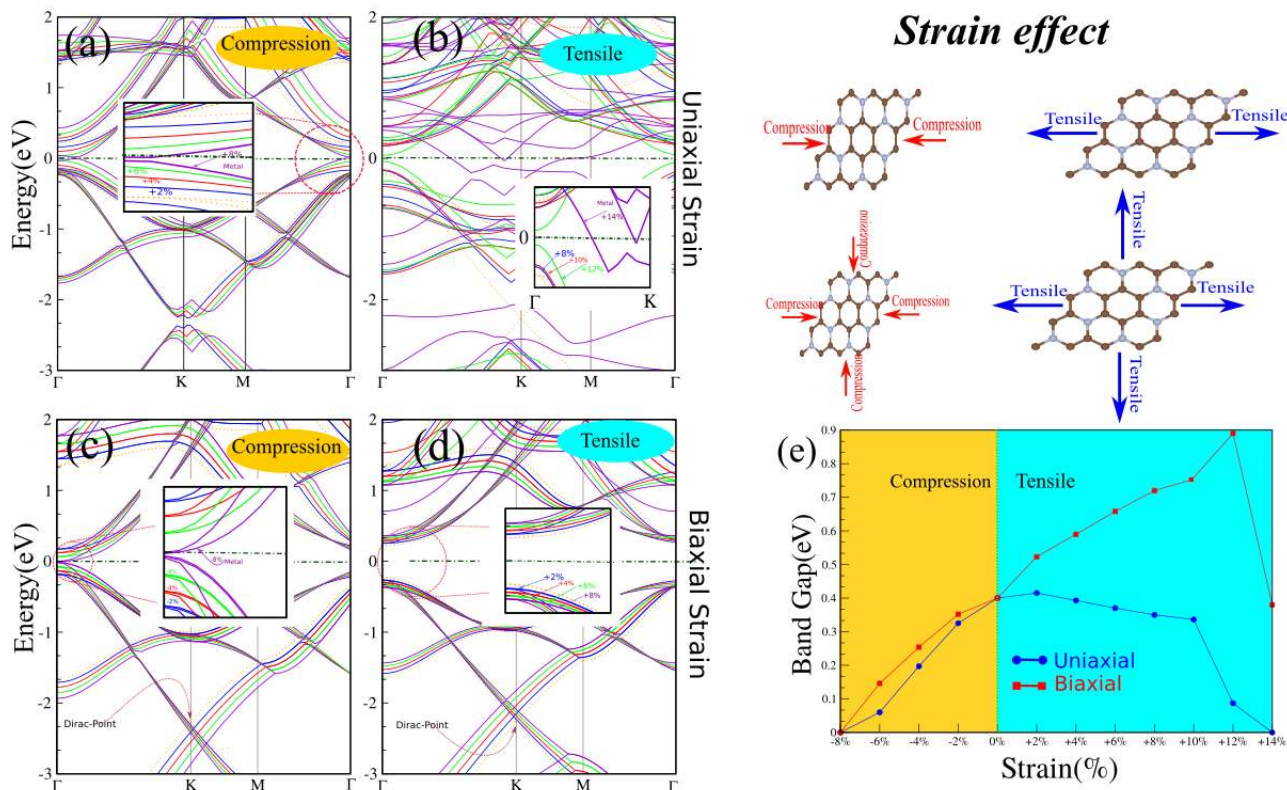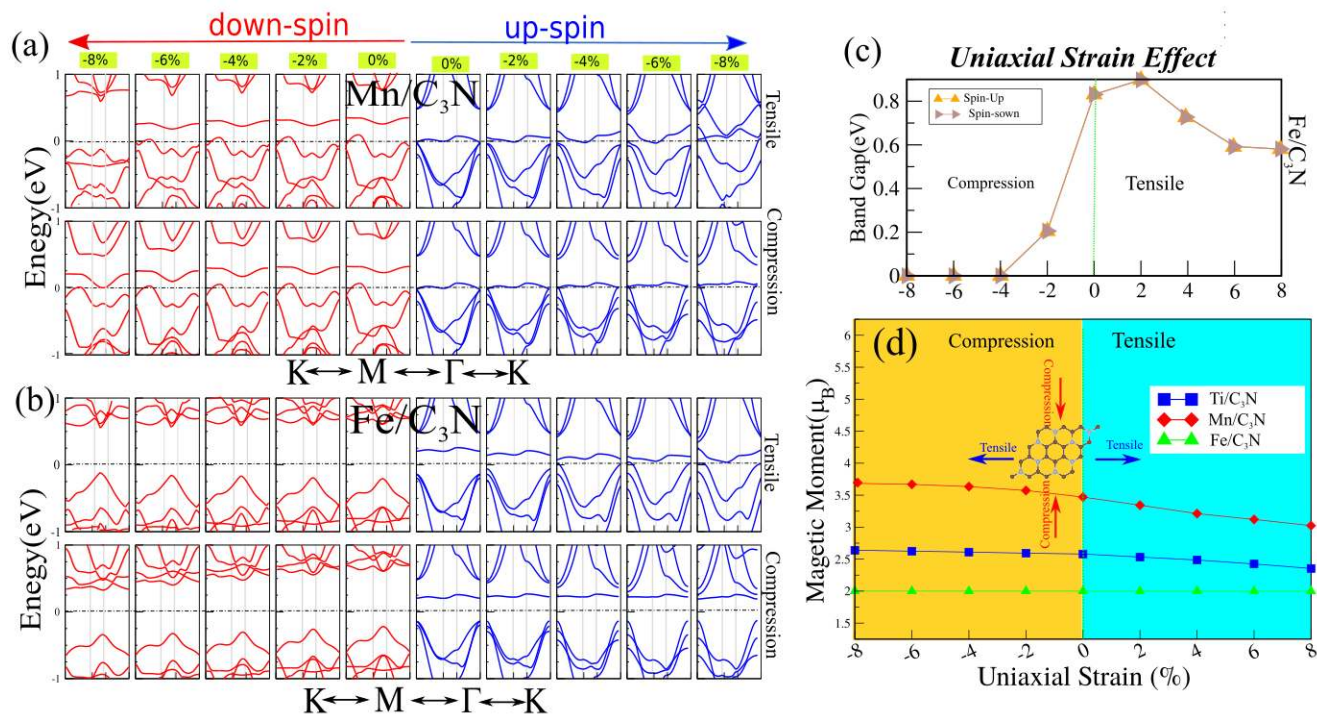
Figure 12: Electronic band structure of C_3N as a function of (a,b) uniaxial strains along zigzag directions and (c,d) biaxial strains The different colored curves correspond with different strengths of strain as indicated on the curves of the insets. The uniaxial and biaxial strain applied on C_3N along ab-axis, are shown at top right. (e) The band gap as a function of uniaxial and biaxial strains. The zero of energy is set to E_F, shown by the green dash-point line.
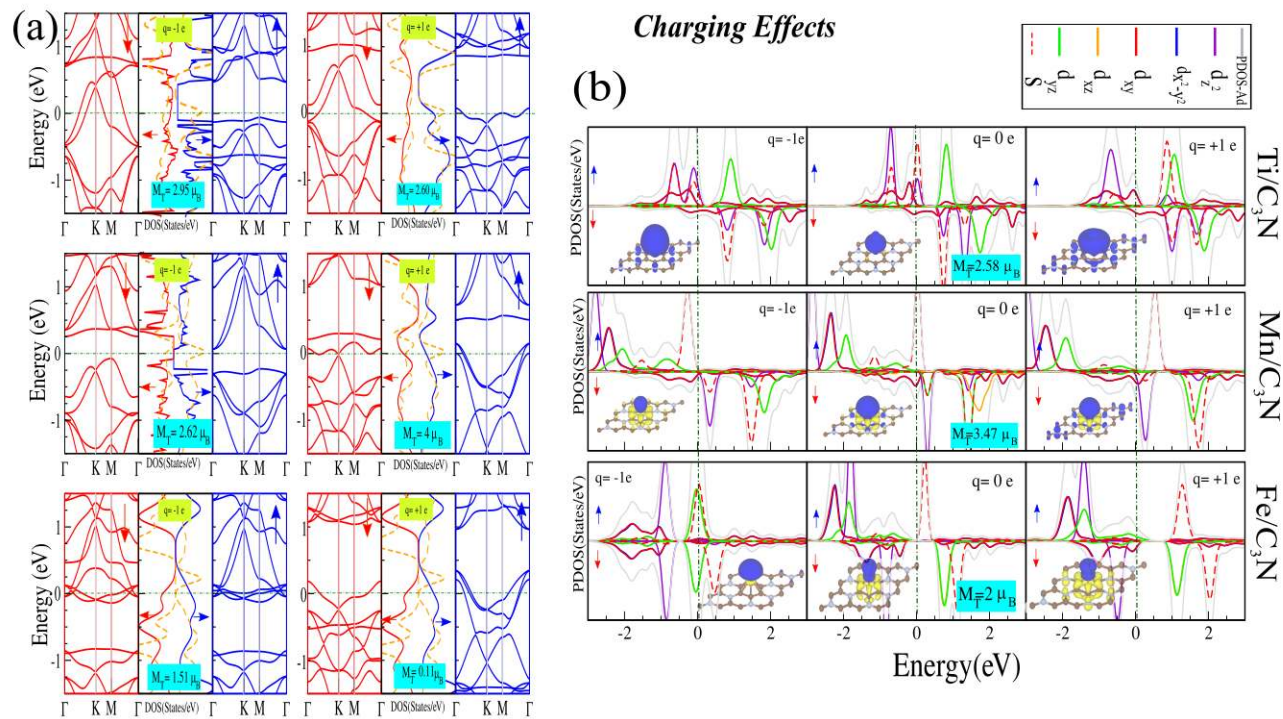
Figure 13: (a) Band structure with DOS and (b) PDOS for Ti, Mn and Fe adsorbed C_3N as a function of charging. The q= +1 e (q= -1 e), corresponds to the charging where one electron is removed (added) to C_3N.
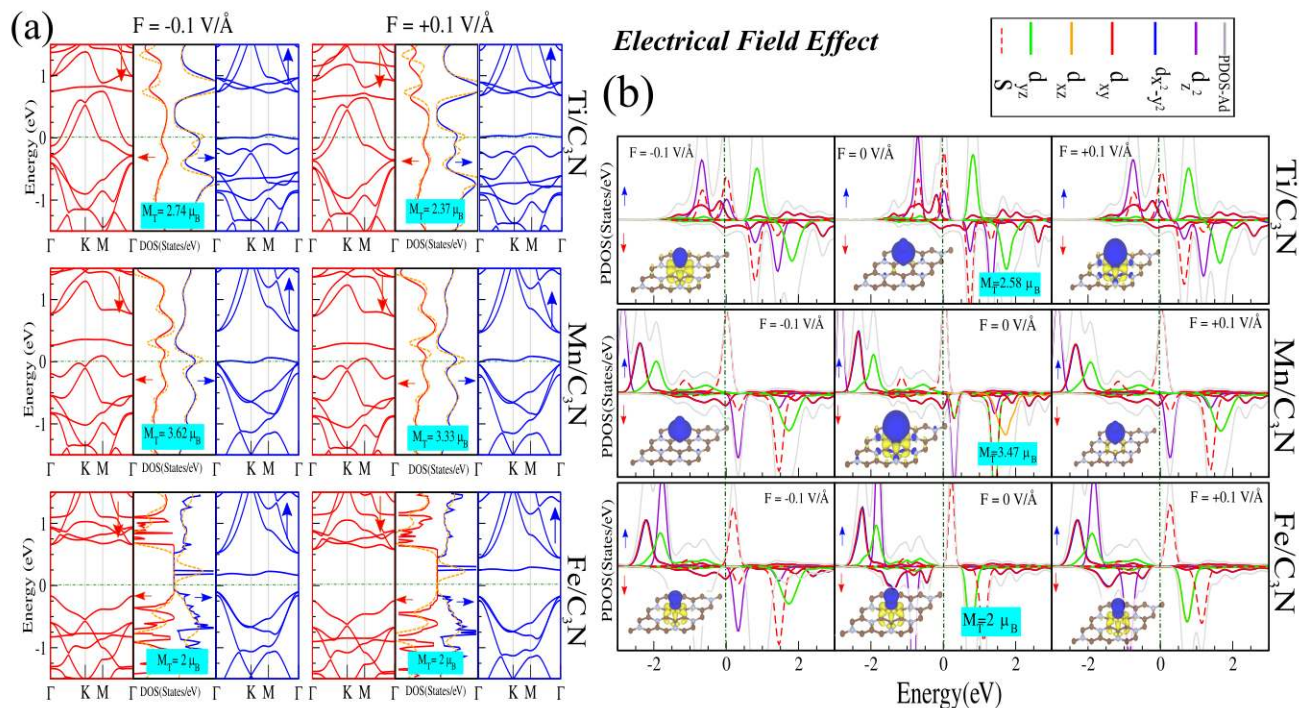
Figure 14: (a) Band structure with corresponding DOS and (b) PDOS for Ti, Mn and Fe adsorbed C_3N as a function of electric field (F). The F= +0.1 and -0.1 V/Å denotes parallel and antiparallel to the z-axis, respectively. The zero of energy is set to E_F, shown by the green dash-point line.

Figure 15: (a,b) Electronic band structure of Mn and Fe adsorbed C_3N as a function of uniaxial strain. (c) Variation of band gap as a function of uniaxial strain for Fe/C_3N. (d) Variation of magnetic moment for the Ti, Mn and Fe/C_3N as a function of uniaxial strain. The zero of energy is set to E_F, shown by the green dash-point line.
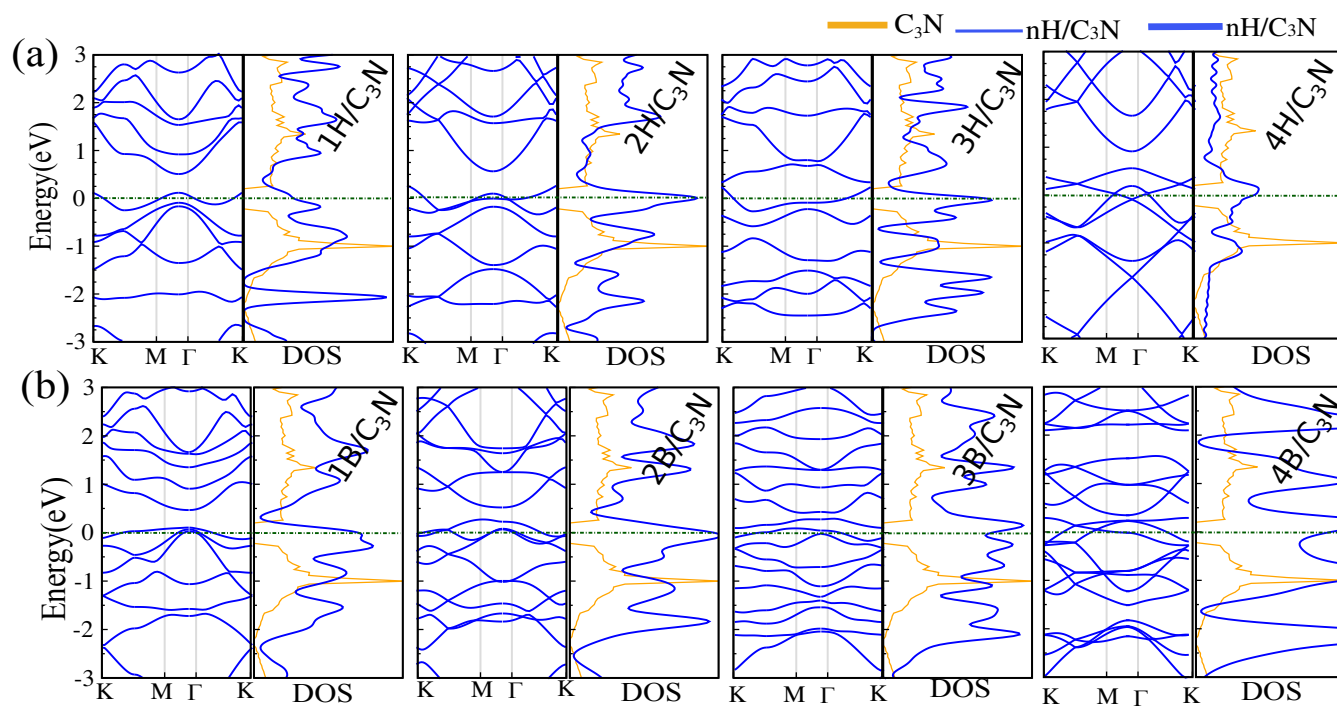
Figure 16: (a,b) Band structure with corresponding DOS of (a) H and (b) B atoms coverage. The zero of energy is set to E_F, shown by the green dash-point line.
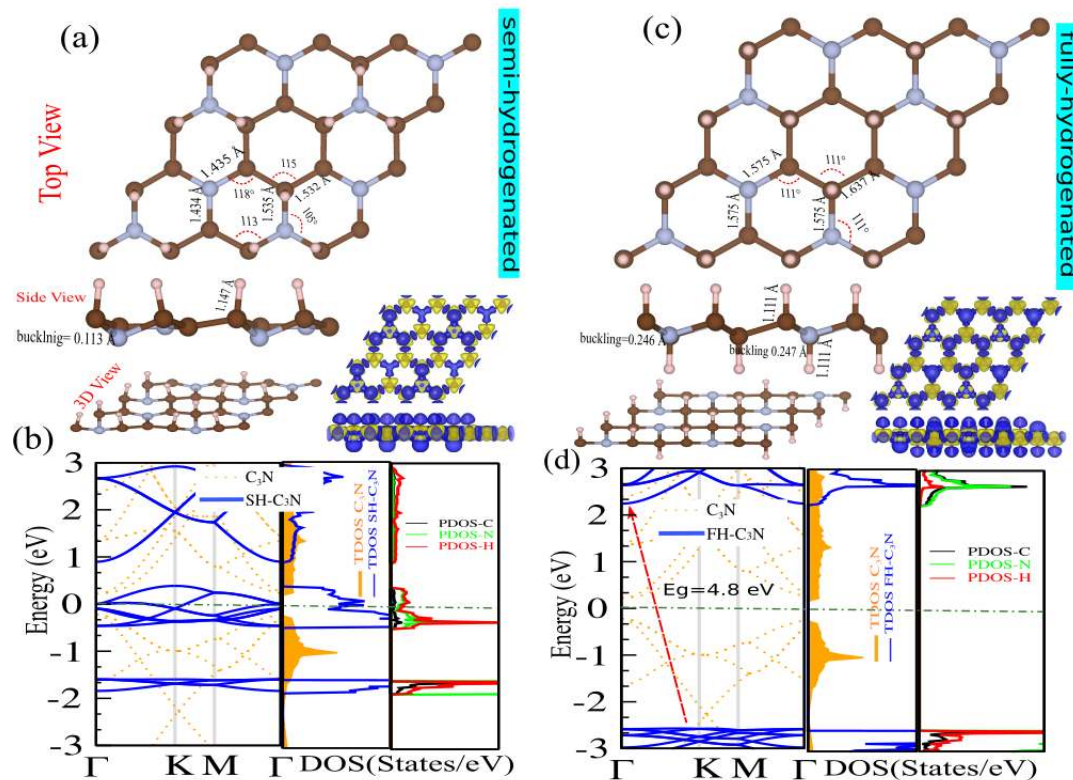
Figure 17: Top and side view of optimized structures, band structure with corresponding DOS and PDOS of the chair-like conformation, (a,b) Semi-hydrogenated C_3N and (c,d) Fully-hydrogenated C_3N. The zero of energy is set to E_F, shown by the green dash-point line. The difference charge density is shown in panels (a) and (c) at bottom-right. The blue and yellow regions represent charge accumulation and depletion, respectively.
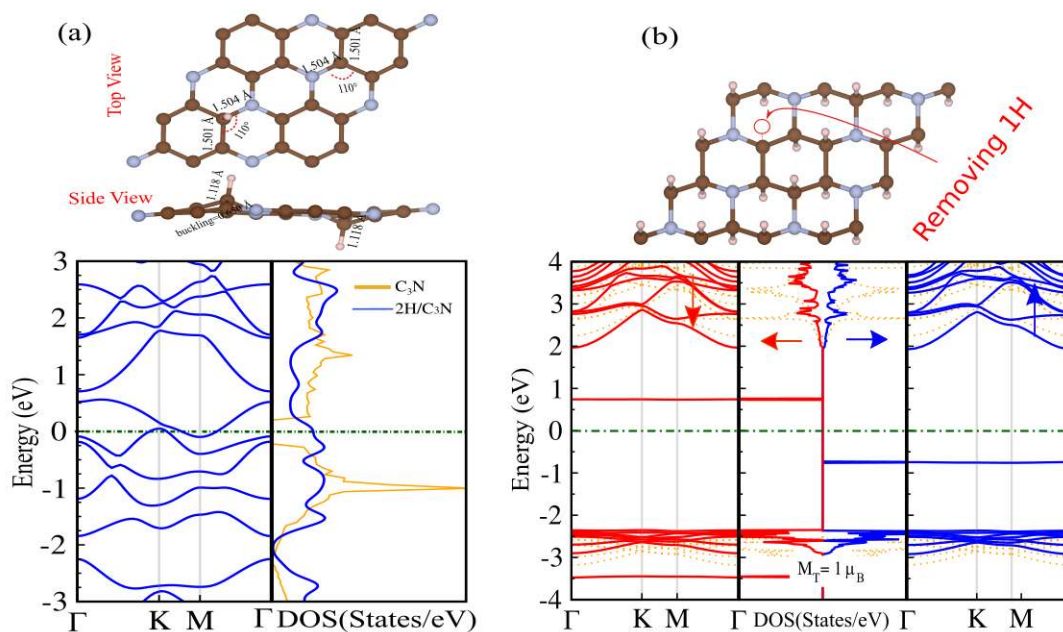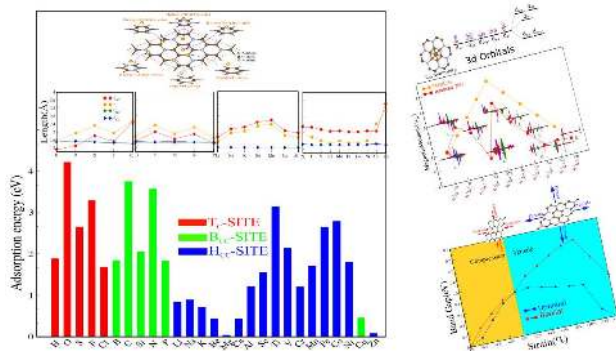
Figure 18: Optimized atomic structure, band structures and DOS of (a) adsorption of two H atoms (show dots) on two-sided of C_3N. (b) Single vacancy of H atom in FH-C_3N. The zero of energy is set to E_F, shown by the green dash-point line.

TOC